2023-XX-XXXX

UAV Icing: 3D Simulations of Propeller Icing Effects and Anti-Icing Heat Loads

Nicolas C. Müller, Richard Hann
Department of Technical Cybernetics, NTNU, Trondheim, Norway

Abstract

In-flight atmospheric icing is a significant threat to the use of unmanned aerial vehicles (UAVs) in adverse weather. The propeller of the UAV is especially sensitive to icing conditions, as it accumulates ice at a faster rate than the wings of the UAVs. Ice protection systems can be developed to counteract the danger of icing on the propeller of UAVs. In this study, the influence of different meteorological conditions on a propeller of a UAV is analyzed for a UAV with a wingspan of a few meters. The ice accretion and the performance degradation and the required anti-icing heat fluxes have been calculated using numerical methods with ANSYS FENSAP-ICE. This analysis has been used to evaluate the critical conditions for the operation of a UAV in icing conditions and the design of a thermal IPS system for a propeller. The highest ice mass has been found at a temperature of −10 °C and an MVD of 20 µm in intermittent maximum icing conditions. The performance degradation has been the highest at lower temperatures of −15 °C in intermittent and at −5 °C in continuous maximum icing conditions. For the design of an IPS, the conditions at the lowest design temperature and the smallest median volumetric diameter (MVD) have been identified as critical points. The most important driver for the required IPS loads on the propeller is the outside temperature, followed by the liquid water content of the cloud. The MVD is important for the distribution of the liquid water content. Here, the highest heat flux required for anti-icing has been computed. The second critical design point is the highest temperature, at an MVD of 40 µm. At this condition, the heat flux is the lowest. This analysis is the basis for the development of electro-thermal IPS for use in UAVs. This paper expands previous research to cover the effect of icing on a propeller of a UAV in a wide range of icing conditions and explains the influence of those conditions on an IPS design.

Introduction

Adverse weather is one of the challenges that unmanned aerial vehicles (UAVs), also called unmanned aerial systems (UAS), drones, or remotely piloted aerial systems, face [1]. One of these adverse weather conditions is atmospheric in-flight icing. Atmospheric in-flight icing is a frequent scenario [2] in large areas of the world [3, 4]. In-flight icing occurs in meteorological conditions where supercooled liquid water exists in the atmosphere. When these supercooled droplets collide with the airframe, they freeze and accumulate over time [5]. The resulting ice accretions can lead to severe aerodynamic performance penalties, especially on unmanned aircraft [6]. Icing is also a hazard to manned aircraft [7] but is a relatively mature research field nowadays [8].

Several studies have been conducted to investigate the negative effects of icing on UAVs. The majority of these studies have used experimental methods to evaluate the aerodynamic penalties on airfoils and wings [9, 10, 11, 12], and some have used numerical simulations [10, 13] The existing literature shows that ice has severe negative effects on lifting surfaces, typically leading to a decrease in the lift, an increase in the drag, and a reduction of stall angles.

The effect of in-flight icing on UAV propellers has even more recently come into the focus of research. Several experimental and numerical studies have shown that icing leads to a very rapid decrease in thrust and performance efficiency, whereas torque is substantially increased [14, 15, 16]. The literature suggests that propeller icing leads to faster and more severe performance penalties compared to icing on lifting surfaces. Therefore, propeller icing significantly threatens UAV operations and deserves in-depth investigations. The icing research on rotating surfaces has been focused on propellers of manned aviation aircraft, rotors of helicopters [17, 18], and wind turbines [19, 20]. The existing research on the icing on rotating surfaces on UAVs is focused on the icing on multi-rotor rotors [21].

On a rotor, the rotation creates centrifugal forces on the accumulated ice on the propeller. If the centrifugal forces are larger than the ice adhesion forces, ice shedding will occur [22]. The process of ice shedding might recover parts of the efficiency of the propeller lost due to icing [23], but the UAV could get damaged by the ice block breaking of the propeller [24], and there is a potential for vibrations if the ice sheds unevenly between the propeller blades. Ice shedding is a stochastic effect and, thus, not always repeatable [23]. The ice shedding can be estimated using analytical methods [25], although experiments performed on the same propeller show a large variation in ice shedding times [23].

In this work, a state-of-the-art CFD solver is used to analyze the ice accretion, performance degradation, and required anti-icing heat flux on the propeller of a UAV in 3D. This analysis is performed at 20 conditions each inside the Appendix C of 14 CFR Part 25 intermittent maximum (IM) envelope and continuous maximum (CM) envelope [26]. The collected data gives insight into the influence of different meteorological conditions on the ice formation on the propeller. With the performance degradation data, the relative severity of icing conditions can be estimated, which is important for decisions related to the optimal path a UAV is flying [27]. Additionally, it is used to estimate the severity of icing conditions on the propeller, which is important to know the safe time a UAV can operate in icing conditions. This is especially important for multi-rotor UAVs, which rely on the thrust from their rotors not only to overcome the drag but also for the control of the UAV and to provide lift. If the rotors lose the ability to produce thrust, they will become uncontrollable and

experience a rapid uncontrolled descent. The change in the performance of the propeller can be used to understand the risk of different icing conditions and to build risk scenarios. This could for example be used as a tool for the path planning for UAV in potential icing conditions [28].

To avoid this issue, a UAV might be equipped with an ice protection system (IPS). Multiple IPS concepts have been developed [29]. Two different methods are used by most of the proposed solutions to protect the propeller of a UAV. The first group is focused on reducing the adhesion between the ice and the propeller with coatings, leading to the process of ice shedding, which limits the ice buildup on the propeller [30, 31, 32]. This reduces the risk of ice accretion on the propeller. The second group is using electricity to heat up the propeller using an electrical heater to prevent ice accretion [33, 34, 35, 36]. This is also called an electro-thermal ice protection system (ETIPS). To design the heater layout of an ETIPS, it is essential to know the required heat fluxes to prevent ice accretion on the propeller. This is a challenge on rotors compared to wings, as the heat fluxes are changing with the chord and the span of the rotor [37]. Using the 3D simulations performed in this study, the required anti-icing heat fluxes were calculated. This data is analyzed to extract the chordwise and spanwise changes in the required anti-icing heat flux. With this data, a heater layout can be selected for an electro-thermal anti-icing system. The results of this study can be used to develop and manufacture an IPS system for a propeller of a UAV.

Similar studies have been performed on the wing of a UAV [10], which indicated that for the wing, the CM envelope is more critical, with a temperature of −2 °C identified as the condition with the strongest influence on the aerodynamic performance of the wing.

The influence of the different meteorological conditions on the required anti-icing heat fluxes is important for the design of a control setup for the IPS system of the UAV. This will allow for an optimization of the required energy for a propeller ETIPS by a better understanding of the required heat fluxes. This is important for the application of UAVs, as the available power for such a system is limited. Furthermore, this will also reduce the thermal loads inside the propeller and thus have a positive impact on the lifetime of an IPS-equipped propeller.

The objective of this work is to analyze the ice accretion of the propeller over a large range of environmental conditions to evaluate the critical conditions which lead to the largest ice accretion, the strongest performance degradation, and the critical design conditions to develop an ETIPS for a propeller of a UAV. The information on the performance influence of the propeller is essential for operators of UAVs to estimate the severity of potential icing conditions.

Methods

The ice accumulation on the propeller is simulated using a state-of-the-art CFD solver. The CFD solver ANSYS FENSAP-ICE Version 2022.2 is used to calculate the ice accretion and performance losses of the propeller in icing conditions, as well as the anti-icing heat fluxes on the propeller.

A propeller with a diameter of 21 inches or 0.533 m has been selected as a representative propeller for small fixed-wing UAVs with a wingspan of around three meters. The propeller used in this study is the 21x13 E propeller manufactured by Mejzlik Propellers [38]. Mejzlik has provided a 3D scan of the propeller, which has been used as the geometry in this simulation. The reference velocity was chosen based on existing flight test data to be corresponding to a flight velocity of 25 m/s and a representative thrust level for level flight. The rotation rate is 4200 rpm.

ANSYS FENSAP-ICE contains three different modules which are used to calculate the ice shape on the propeller of a UAV. FENSAP is a finite element flow solver that is utilizing Reynolds-averaged Navier-Stokes equations [39]. The flow solution of FENSAP is used by DROP3D to calculate the droplet distribution and the impingement of the droplets on the propeller. DROP3D is using an Eulerian approach to calculate the droplet distributions [40, 41]. The ice accretion is calculated by the module ICE3D [42, 43]. This module is using the Messinger approach to calculate the heat flux balance on the surface and subsequently to calculate the ice accretion [44].

In FENSAP-ICE, a Spalart-Allmaras turbulence model without transition has been used to calculate the airflow of the propeller. The rotation is simulated as a rotating reference frame. In DROP3D, the vapor model is used, with a relative humidity of 100% assumed. In ICE3D, the heat transfer coefficient is calculated with the extended icing data mode, as this is the only one that allows for the calculation of heat fluxes in FENSAP-ICE with rotating bodies. The extended icing data mode is a proprietary technology by ANSYS that calculates the heat transfer coefficients based on the flow solution from FENSAP. The surface roughness is modeled using the sand-grain roughness method with roughness values calculated in ICE3D based on the calculated ice shape with an included beading module. This model calculates the roughness values based on the water beading on the local conditions.

A half cylinder has been used as a computational domain in the simulation setup. The second propeller blade has been simulated by the use of rotational periodic interfaces, which reduces the number of cells in the mesh by half. The computational domain has a diameter of five times the propeller radius. It has an extent of five times the radius towards the front and ten times the radius towards the rear of the propeller. The mesh is created with Fluent Meshing, using a hybrid grid with up to 37 prism layers. The initial layer height is 0.05 mm to ensure a y-plus value smaller than one over the entire surface of the airfoil. A volumetric refinement zone with the radius of the propeller extends from the plane of the propeller in the direction of the airflow. This is used to resolve the propeller wake.

There are two methods of estimating the required anti-icing heat loads of the propeller required to keep the propeller ice-free. The running wet mode calculated the heat load to keep the surface of the propeller ice-free. The fully evaporative mode calculated the required heat flux to evaporate all the impinging water on the surface of the propeller. This mode does not include the running back of the water, and requires a smaller heated area, although the anti-icing powers are increased.

The simulation conditions have been chosen according to the certification parameters and Appendix C of 14 CFR Part 25 [26]. The meteorological conditions are chosen from the IM and the CM envelope. For each envelope, four MVDs and five temperatures are calculated. The simulated conditions can be seen in Fig. 1. The IM conditions are shown in Tab.2, and the CM conditions are shown in Tab. 3.

For the selection of the ice accretion time, multiple factors had to be considered. On the propeller, the ice accretion occurs at a rate that leads to ice shedding or negative thrust values within a few minutes [23]. Therefore, choosing the flight time of the UAV through a cloud of the extent specified by the IM and CM envelopes is not a good representation of the performance impact of icing on the propeller. Previous experiments of icing effects on the propeller in this study [23] have shown that the propeller might generate negative thrust values within 2 minutes of ice accumulation. For the estimation of the relative performance impact of ice accretion, extending the ice accretion time longer is not beneficial, as this might have an effect on the gradient of the performance degradation over time. Another effect influencing the appropriate ice accumulation time is ice shedding. This describes the process of ice breaking of the propeller due to mechanical or aerodynamic forces. The main factor for ice shedding

Table 1: Parameter setup for the ice accretion simulation.

FENSAP	
Turbulence model	Spalart-Allmaras
Boundary layer	Fully turbulent
CFL number	150
Time steps	800
Artificial viscosity	Streamline upwind + cross wind dissipation 1E−07
DROP3D	
Physical model	Droplets
Relative humidity	100%
Distribution	Monodisperse
Water density	1000 kg/m^2
ICE3D	
Ice - Water model	Glaze Advanced
Extended Icing data	Activated
Roughness output	Sand grain from beading
Time step	Automatic
Grid displacement	12 shot multishot, custom Fluent Meshing

is the balance between the ice adhesion and the centrifugal forces' action on the propeller. Ice adhesion depends on ambient air temperature, and generally lower temperatures lead to higher ice adhesion forces [23].

A short ice accretion time has been chosen to provide representative ice shapes on the propeller, which enables the assessment of the speed of the performance degradation of the propeller. The ice accretion time is 30 s for the IM conditions and 180 s for CM simulations. This is based on previous experimental work on the propeller in an icing wind tunnel (IWT) [23]. In the experimental research, icing experiments in a controlled environment were performed to analyze the impact of icing on performance degradation.

A multi-step ice accretion simulation is used to assess the performance penalties. After each time step, a new mesh is created with Fluent Meshing [45]. The meshes are created with the same settings used in the original mesh creation. This leads to similar meshes over the time steps, where only the ice shape is different. The number of cells in the mesh will increase with the iterations. This increase is caused by the ice shapes increasing the surface area of the propeller and the more complex ice shapes increasing the curvature of the meshed surface, thus reducing the cell sizes. This is due to a curvature refinement used to define the mesh sizes in the meshing process. This leads to an increase in the number of cells from 20 million in the clean mesh up to a maximum of 45 million in the base mesh. A section of the base mesh at 75 % of the radius can be seen in Fig. 2. An image of the propeller with its surface mesh can be seen in Fig. 3, showing the size of the cells on the spinner and the propeller surface. Two additional meshes were created, one where each grid size was reduced by a factor of $\sqrt{2}$ for a finer mesh resolution, and a third mesh with an increased grid sizing by a factor of $\sqrt{2}$ for a coarse mesh. For the validation of the results, the CM case at −5 °C and an MVD of 15 µm was calculated with all three meshes. This case was chosen as with the highest LWC, it has the largest potential for ice to form, and glaze ice shapes, which are more common at lower temperatures also show the largest variations. Therefore, this case is expected to highlight some of the largest differences between different meshes.

The number of time steps has an almost linear influence on the simulation time because it determines the number of flow simulations necessary which is the longest step during the ice accretion calculation process. Therefore, the number of time steps is an important factor in conducting the simulations efficiently with a manageable amount of computational effort. For this reason, a time-step sensitivity calculation has been performed, in which the number of time steps is varied. One simulation is performed with 11-time steps and one with

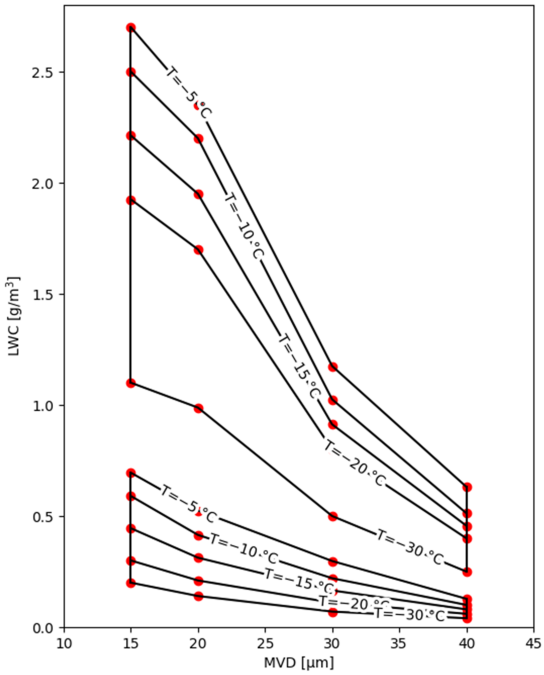

Figure 1: Selected conditions for analysis in the intermittent maximum and continuous maximum envelope. The upper area represents the CM, and the IM envelope is the lower area.

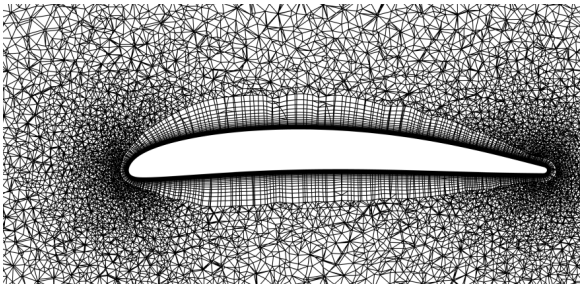

Figure 2: Section of the medium mesh for the 3D simulation at 70% of the radius.

21-time steps. In both cases, the first two time steps are shorter than the following time steps, to achieve a higher resolution in the initial ice accretion. The first time step has a third of the length of the regular time steps, and the second two-thirds so that they have the same length as one conventional time step. The simulations are based on the CM simulations at −5 °C and an MVD of 20 µm, as this is expected to see the largest ice mass on the propeller and the formation of horn ice shapes which are more complex to resolve and thus will be more influenced by an increase in the temporal resolution [10].

To analyze the heat loads, three different analysis methods are used. The first method looks at the peak heat flux of a chordwise section [46]. This is usually near the stagnation point of the airfoil. This can be used to evaluate the change in the heat flux across the span of the propeller. The second method is looking at the heat flux integrated over a small section of the leading edge, where a heating element could be placed. The size is determined based on the results for the chordwise heat flux distribution and can thus only be performed after the simulations are done. Lastly, the heat fluxes are integrated over the entire surface of the propeller. This allows for a

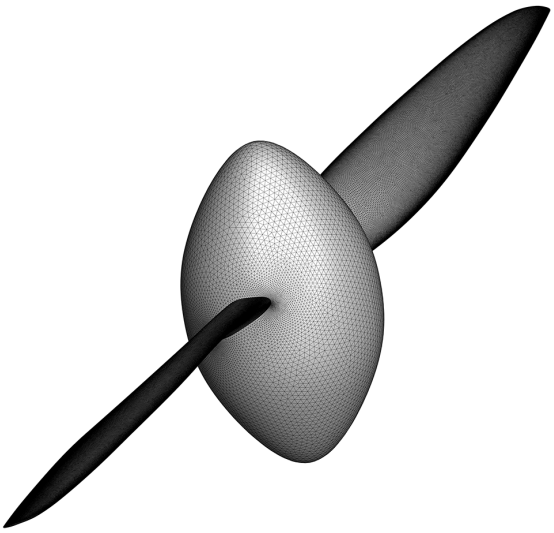

Figure 3: Surface mesh of the propeller in the base mesh.

comparison of the heat flux requirements for an idealized heating element which provides exactly the heat flux distribution that would be required. While a heating element with this ideal heat flux distribution is not realistically achievable for all the conditions, it allows for a comparison of the severity of different conditions without the bias of a selected heating element layout.

The results have been plotted using contour plots over the calculated envelopes. TO interpolate between the plots, a structured mesh was generated, consisting of triangles. One side of the triangle is aligned with the iso-temperature lines, and another with the MVD. The third side is crossing the resulting shape by going from the point with The lowest MVD and temperature to the point with the higher MVD and temperature. As all the iso-temperature lines are monotonous decreasing in LWC with increasing MVD, this creates the diagonal which is closer to having a constant LWC. The created mesh can be seen in Fig. 4. All values are linearly interpolated along the lines, and linear interpolation is also used to fill the area between. This special mesh was chosen as it allows for an accurate representation of a value that has a gradient with the temperature or the MVD. Gradients for constant LWCs might be affected by the choice of interpolation, but with the choice for meteorological conditions inside the IM and CM envelopes, multiple simulations with constant LWC are not calculated. For the analysis at multiple sections, cross sections at 30%, 50%, 70%, and 90% were used. For the analysis of single sections, the cross-section at 75% was used, as an analysis of the spanwise thrust generation has shown that this section contributes the most to the thrust of the propeller. All data points presenting integrated values for the entire propeller are multiplicated by a factor of two to represent the full propeller and not only a single propeller blade.

Results

In this section, the results from the numerical analysis are shown. First, the convergence studies runs are shown, then the ice shapes and the performance results are shown. Lastly, the required anti-icing heat fluxes for a thermal IPS are presented.

Convergence study

During the mesh convergence study, the finest mesh was only able to calculate seven time steps representing half the ice accretion time, until the increased memory requirements of the increasing cell number prevented the continuation of the simulations. The results from the first six steps of the mesh convergence study are shown in Fig. 5. All three meshes seem to generate similar ice shapes, with

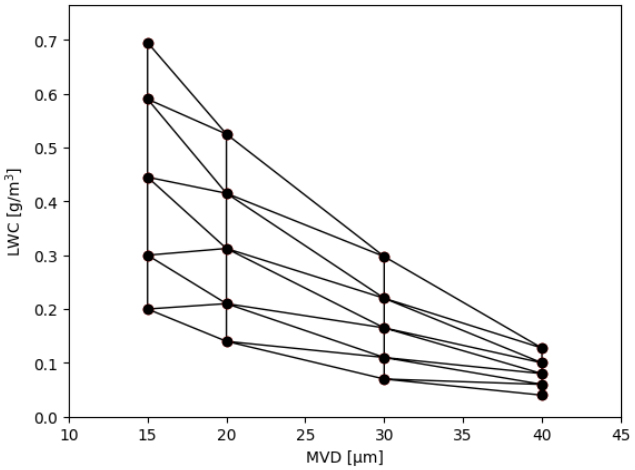

Figure 4: Mesh used for plotting the results over the CM envelope

small differences on the end of the ice layer on the top surface of the propeller, and a slight reduction of ice horn height on the lower surface close to the stagnation point of the propeller. For the purposes of this study, the differences are minimal, and thus it was chosen to continue only with the base mesh and the coarse mesh.

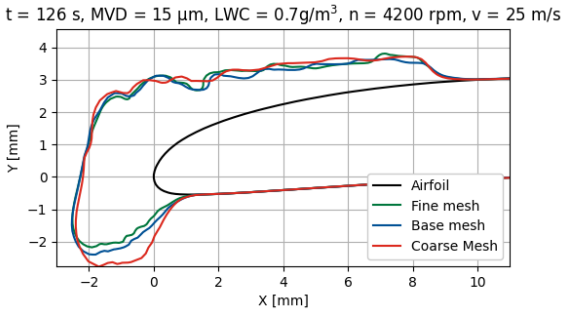

Figure 5: Results of the mesh study in CM conditions at −5 °C and an MVD of 15 µm after 126 s of icing conditions, the ice shapes are taken at 75% of the propeller radius.

The ice shapes after 180 s of ice accretion between Mesh 2 and Mesh 3 can be seen in Fig. 6. After 12 Steps, a difference in the lower ice horn is visible, with a lower horn angle and horn height for the base mesh. This combined with the slight increase in the upper horn height led to an increase in ice mass for the coarse mesh over the base mesh. The ice thickness at the leading edge of the airfoil is similar, with a small reduction in the coarse mesh. The icing limits are the same for both meshes.

The extracted thrust is 7.30 N without ice, and 0.65 N after 180 s of icing for the coarse mesh. For Mesh 2, the thrust is 7.55 N clean and 0.56 N after 180 s of icing conditions. The thrust of the propeller with the fine Mesh 1 is 7.59 N. With the small difference in thrust between Mesh 1 and 2, Mesh 2 was chosen for the remaining study.

The first step in the validation of the required ice shapes was to evaluate the need for a multi-step simulation. In Fig. 7, the ice shapes of the propeller are shown, once with a single-step ice accretion simulation and once with an 11-step multi-step simulation. Between bot simulations, a significant difference can be seen in the calculated ice shapes. The single-step simulation is not predicting the formation of an ice horn. Furthermore, the icing extent on the upper and lower surfaces of the propeller is larger for the single-step simulation. Lastly, the ice thickness is reduced for the single-step simulation on the leading edge, but greater on the top and lower surface. For this reason, for the remaining simulations, a multi-step simulation

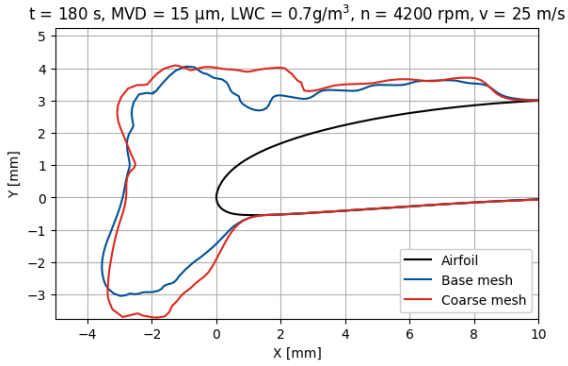

Figure 6: Results of the mesh study in CM conditions at −5 °C and an MVD of 15 µm after 180 s of icing conditions. The ice shapes are taken at 75% of the propeller radius.

approach was chosen.

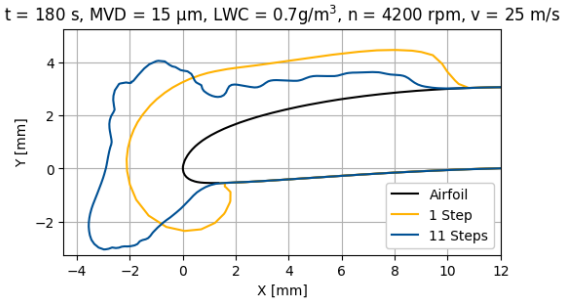

Figure 7: Comparison of a single step and a multi-step simulation at −5 °C and an MVD of 15 µm, the sections are taken at 75% of the propeller radius.

The validation of the icing steps can be seen in Fig. 8. In this comparison, the runs show very similar ice shapes. The icing extent is similar between both simulations. Also, the ice thickness at the leading edge at the height of $y = 0$ mm is similar between both simulations. The main difference between the simulations is in the lower ice horn. This is sharper for the 21-step simulation compared to the 11-step simulation, indicating that the resolution of such fine details is better resolved with more simulation steps. As the difference is small between both simulations and taking into account that the difference is likely to be less for simulations with higher freezing factions and thus fewer horn ice shapes, 11 steps were used in the remaining simulations. The slight improvement in capturing the horn ice shape is not worth the additional computational cost of the 21-step simulation.

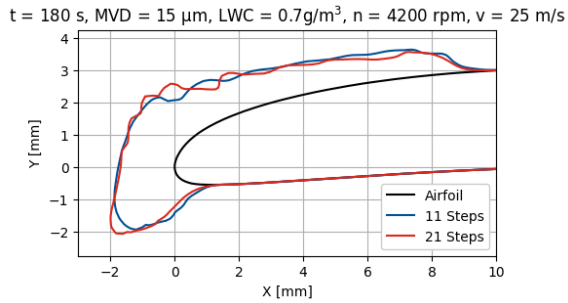

Figure 8: Results of the time steps simulation in CM conditions at −5 °C and an MVD of 15 µm, the sections are taken at 75% of the propeller radius.

Ice accretion results

The ice shapes are analyzed at multiple spanwise sections across the propeller. In Fig. 9 and Fig. 10, the ice shapes are shown at a section of 70% of the radius of the propeller in IM and CM conditions for an MVD of 15 µm. The ice shapes for the remaining CM cases and additional IM sections can be seen in Appendix B.

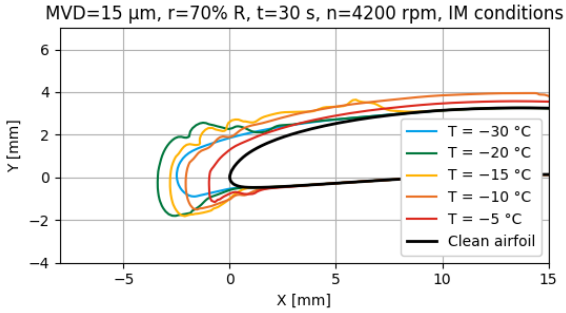

Figure 9: Ice shapes obtained by 3D simulations on the propeller for cases with an MVD of 15 µm after 30 s ice accretion in IM conditions.

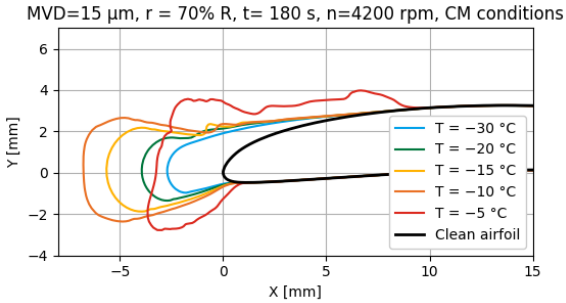

Figure 10: Ice shapes obtained by 3D simulations on the propeller for cases with an MVD of 15 µm after 180 s ice accretion in CM conditions.

All ice shapes except for the simulation at −5 °C are streamwise ice shapes in CM conditions. At the higher LWC in IM conditions, only the ice shape at −20 °C is a typical streamwise ice shape, while the other ice shapes present horns. The maximum ice thickness can be observed at an MVD of 15 µm in IM conditions at −20 °C. IM CM conditions, the maximum ice thickness is observed at −10 °C. The ice extent is also different between the cases. The ice extent on the top surface is larger than on the bottom of the propeller. The icing extent can be seen in Fig. 11, and is generally observed to be larger with higher temperatures. The ice shapes are also changing with the different conditions.

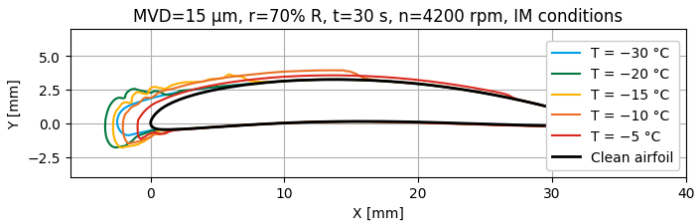

Figure 11: Wider view of the ice shapes obtained by 3D simulations on the propeller for cases with an MVD of 15 µm after 30 s ice accretion in IM conditions.

In Fig. 12, the distribution of the ice mass in IM conditions is shown. The ice mass changes with the temperature, the MVD, and the LWC. The ice mass appears to be proportional to the LWC. At higher temperatures and LWCs, the ice mass is no longer only dependent on the LWC. The ice mass on the propeller is reaching a peak at −10 °C and an MVD of 20 µm.

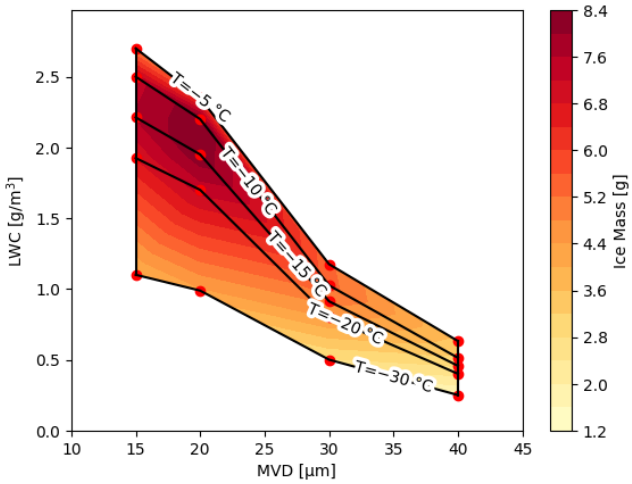

Figure 12: Ice mass on the propeller during the for 3D simulations for all cases within the IM envelope after 30 s of icing conditions.

The same can be seen in Fig. 13 for the CM envelope. The ice mass distribution is shifted towards lower MVDs than the IM envelope. The maximum ice mass is now at an MVD of 15 µm and a temperature of −10 °C. In general, the mass of the accumulated ice appears to show the strongest correlation to the LWC.

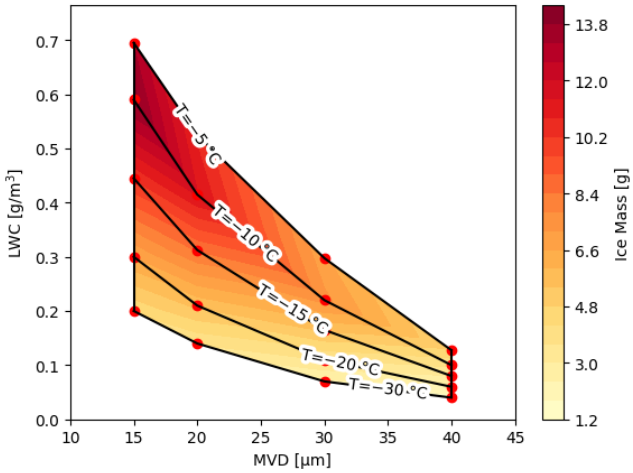

Figure 13: Ice mass on the propeller during the for 3D simulations for all cases within the CM envelope after 30 s of icing conditions.

A factor that is used to classify the ice shapes on the propeller is the freezing fraction. A freezing fraction of one will lead to a rime ice shape, typically streamwise, and a glaze ice shape typically has lower freezing fractions. To classify the different ice shapes on the propellers for the different meteorological conditions, the freezing fraction on the leading edge of the propeller airfoil at 75% of the radius is presented in Fig. 14 for IM conditions and in Fig. 15 for CM conditions. In both envelopes, the freezing fraction decreases with increasing temperatures, an increase in LWC, and a decrease in MVD. At −30 °C in the CM envelope, a freezing fraction of one is observed for all temperatures. In the IM envelope, even at −30 °C the freezing fraction is not one at an MVD of 15 µm and 20 µm. This difference in the freezing fraction can explain the difference in the ice shapes between the CM and the IM simulations, with more streamwise ice shapes in the CM simulations and an increased tendency for horn ice shapes in the IM envelope.

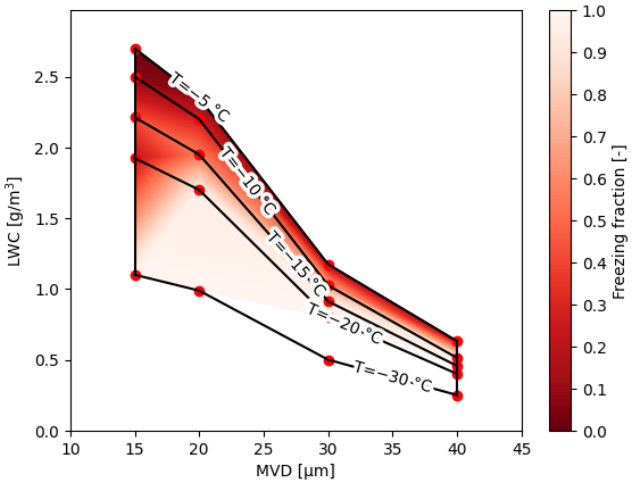

Figure 14: Freezing fraction on the stagnation point of the propeller at 75% of the radius of the propeller in IM conditions.

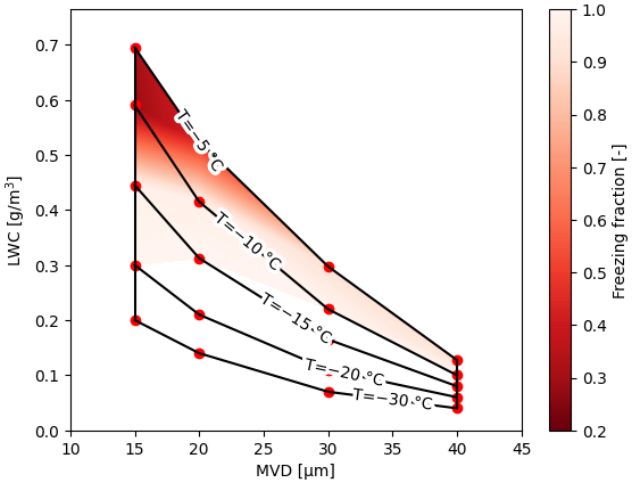

Figure 15: Freezing fraction on the stagnation point of the propeller at 75% of the radius of the propeller in CM conditions.

Performance of the iced propeller

For the calculated ice shapes, the performance of the propellers has been calculated. In IM conditions, the thrust of the propeller is shown in Fig. 16. In most simulations, the thrust is negatively impacted by the ice accretion. The most significant thrust reduction can be observed at temperatures of -15 °C, and for an MVD of 20 µm. This corresponds to areas with a high ice mass, and a medium freezing fraction. At a temperature of −30 °C and an MVD of 30 µm and above, the propeller shows an increase in thrust compared to the clean propeller, which is generating a thrust of 7.5 N. This could be caused by a streamwise ice shape that is increasing the surface area of the propeller and thus allows for more thrust generation. For streamwise ice shapes, this could offset the lift reduction by the change in the airfoil and the increased surface roughness. These results are consistent with experimental results performed on the same propeller geometry, which were conducted at similar temperatures, but different LWCs and MVDs [23, 47].

The torque of the propeller after being exposed to IM icing conditions is shown in Fig. 17. The torque of the propeller is the largest at −15 °C. This contrasts with the thrust degradation, where the worst case is at −10 °C. Again, droplet diameters of 15 µm and 20 µm have the largest influence on the torque of the propeller. Higher

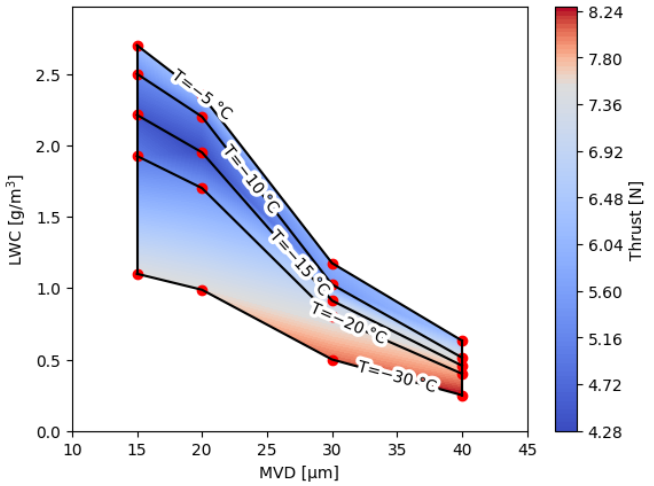

Figure 16: Thrust of the propeller after being exposed to IM icing conditions for 24 s.

temperatures show only a limited increase in torque. Additionally, the area of the most significant torque increase is occurring at smaller droplet sizes, with droplets of 30 µm MVD and above only displaying a small increase in the torque of the propeller. At an MVD of 40 µm, the torque increase is limited to less than 10%. However, it is expected that this torque increase would continue for longer icing durations.

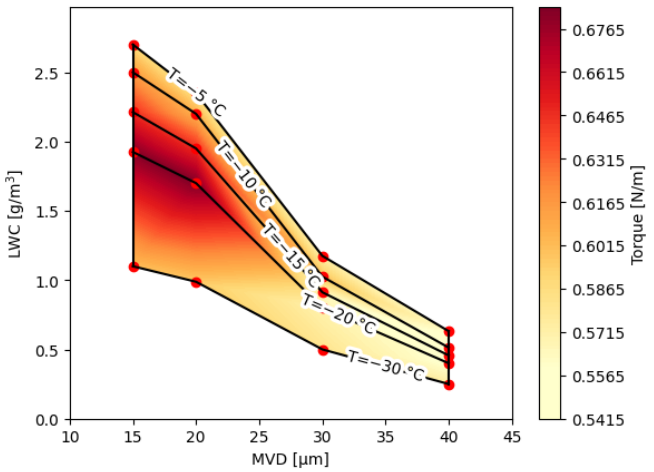

Figure 17: Torque of the propeller after being exposed to IM icing conditions for 24 s.

The total efficiency of the propeller after being exposed to IM conditions is shown in Fig. 18. The performance degradation is dominated by the thrust degradation, shown in Fig. 16. Again, the main correlating factor is the LWC for larger droplet sizes and the strong temperature correlation at higher temperatures, and with smaller droplet sizes. The worst case for the icing of the propeller in IM conditions is an MVD of 20 µm and a temperature of −15 °C, with an efficiency of 37.5% after 24 s of icing conditions.

In Fig. 19, the thrust of the propeller in CM conditions after 180 s of icing is shown. This plot shows that the thrust the propeller is producing in icing conditions is most strongly correlated to the LWC. At a temperature of −5 °C, the propeller is no longer producing any thrust but is generating drag. At a temperature of −30 °C and an MVD of 40 µm, the propeller is generating more thrust than the propeller outside of icing conditions. The plots showing the efficiency and the torque changes are in Appendix C.

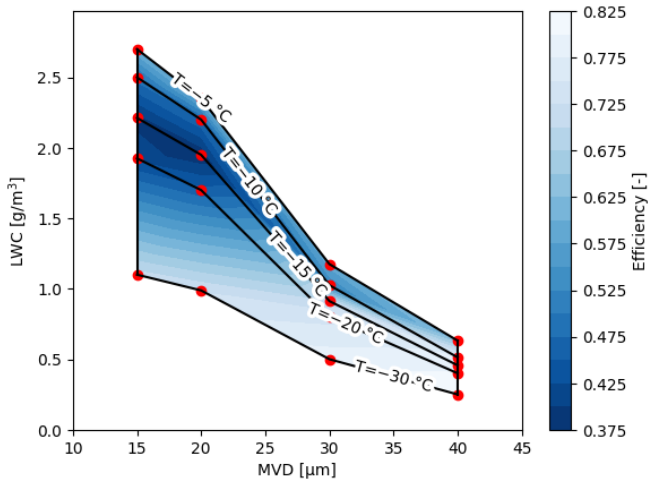

Figure 18: Efficiency of the propeller after being exposed to IM icing conditions for 24 s.

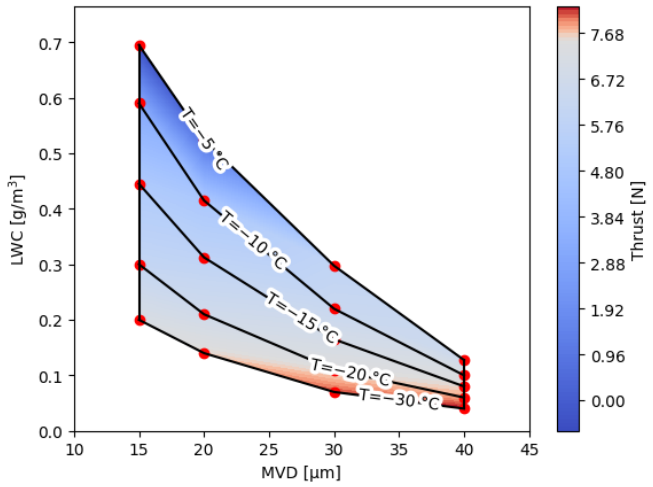

Figure 19: Thrust of the propeller in CM icing conditions after 180 s of icing conditions.

The time evolution of thrust and torque is shown in Fig. 20 for the most critical condition in the CM envelope at −5 °C and with an MVD of 15 µm. In this figure, it can be seen, that the thrust of the propeller decreases almost linearly during the ice accretion duration. The calculation after 162 s is the first, in which the propeller generates a negative thrust value. The torque of the propeller increases in a similar linear fashion during the simulation duration. After 180 s, the propeller requires a torque value of 179% of the initial value, which implies an average torque increase of 0.44% per second during the ice accretion time. The thrust is reduced by 0.60% per second on average during the simulation duration.

Anti-icing heat fluxes

In this section, the anti-icing heat fluxes are shown. The anti-icing heat fluxes are calculated for the clean propeller in the first step of the ice accretion simulation. First, the results for the chordwise, then the spanwise heat flux distribution are shown. Then, the variations of the heat fluxes are shown over the simulated envelopes.

Chord-wise variation of the heat fluxes

The required running-wet anti-icing heat flux varies across the chord of the propeller. Fig. 21 shows the heat fluxes displayed over the

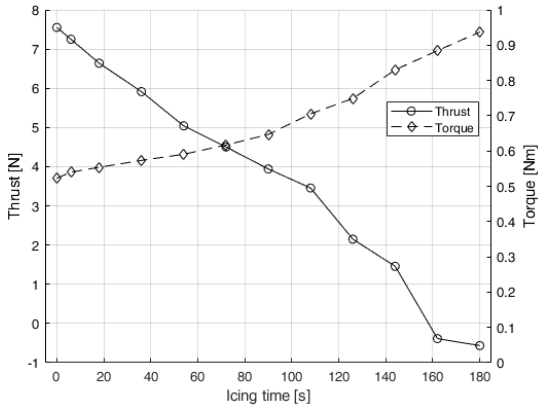

Figure 20: Thrust and torque of the propeller over ice accretion time in CM conditions at −5 °C and with an MVD of 15 µm.

dimensionless wrapping distance along the propeller. The wrapping distance is defined as positive along the top surface of the airfoil, and negative values indicate the lower surface of the propeller. The value of zero is placed at the leading edge of the airfoil. The plot shows that the heat flux has a peak close to the leading edge of the propeller. The heat flux is decreasing rapidly from this. The propeller shows a minimum heat flux on the lower surface of the propeller, which is correlated with a separation bubble in the same position. On the top surface, the heat flux decreases monotonously. With increasing temperatures, the required anti-icing heat flux is decreased. The general shape of the heat flux distribution stays the same. In Fig. 22, the heat flux distribution for the highest MVD of 40 µm is shown. Here, the heat flux distribution around the leading edge of the propeller is similar to the heat flux at an MVD of 15 µm, but the general level is lower. The respective values for the CM envelope are shown in Appendix D.

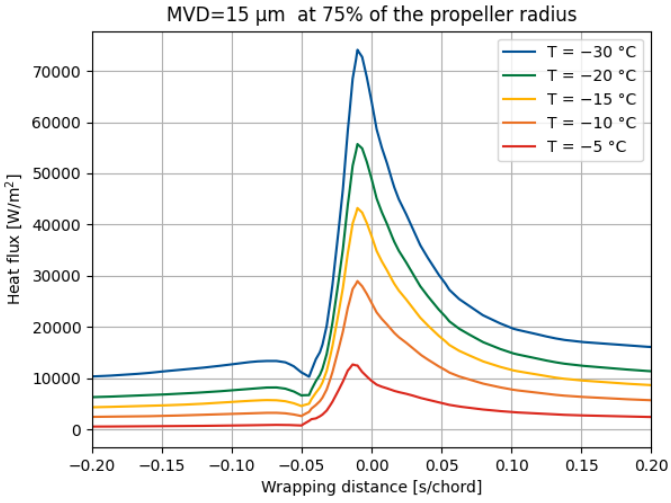

Figure 21: Running-wet heat flux on the propeller for cases with an MVD of 15 µm in the IM envelope.

Span-wise variation of the heat fluxes

The heat flux of the propeller is varying across the span of the propeller. It can be seen in Fig. 23. In the figure, the variation of the peak anti-icing heat-flux over the span of the propeller is shown. The peak heat flux is showing a linear increase in the range between 25% and 65% as well as between 80% and 95% of the radius of the propeller. The reduction in the peak heat flux between 65% of the

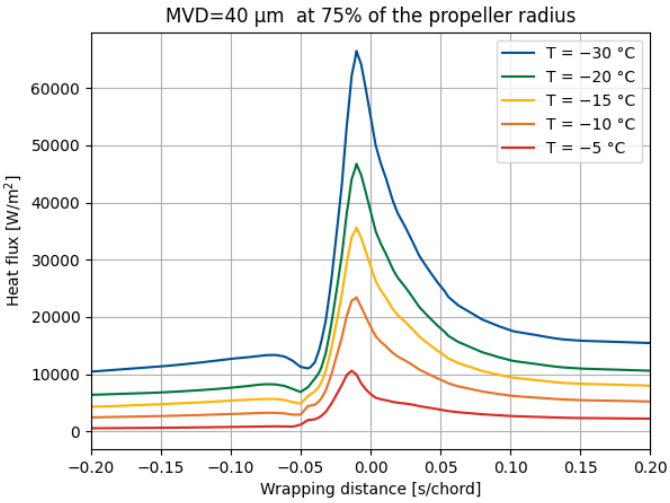

Figure 22: Running-wet heat flux on the propeller for cases with an MVD of 40 µm in the IM envelope.

radius and 80% of the radius correlates with a change in the airfoil of the propeller. The airfoils at 65% and at 80% of the radius of the propeller can be seen in Fig. 24. The airfoil at 80% has a larger leading edge radius compared to the airfoil at 65% which could explain the reduction in the peak heat flux. Or the simulation in IM conditions at −10 °C and an MVD of 20 µm is shown. Additionally, the integrated heat flux over the width of an idealized heating element is shown in Fig. 23, which has a width of 1 mm below the leading edge and 5 mm above the leading edge. In this plot, the heat flux is increasing in a linear fashion from the center of the propeller to the tip of the propeller. The gradient is smaller than the change of the peak heat flux. There is no visible change in the integrated heat flux over the heating element where the airfoil is changing.

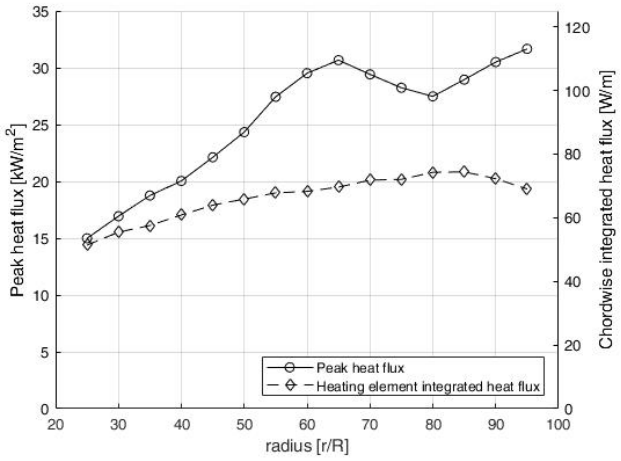

Figure 23: Peak and over the heating element integrated running-wet heat flux on the propeller over the radius of the propeller in IM conditions at −10 °C and an MVD of 20 µm.

This heating element integrated heat flux is shown in Fig. 25 at an MVD of 20 µm for multiple temperatures over the IM envelope. It can be seen, that in general, lower temperatures lead to higher running-wet heat fluxes. Additionally, the gradient of the heat fluxes changes with the temperatures. While the heat fluxes at −10 °C and colder show a linear monotone increase in the heat flux with the radius to a maximum at 85% of the radius and then a small decline, at −5 °C, the increase is minimal. It finds its maximum at 55% of the radius and is then decreasing again, to its minimum at 95% of the radius.

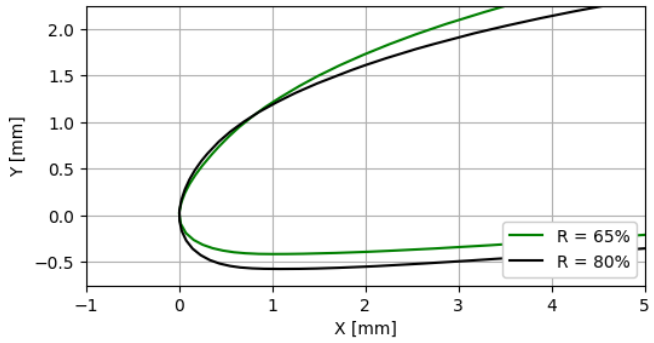

Figure 24: comparison of the leading edge of the airfoil at 65% of the radius and 80% of the radius of the propeller.

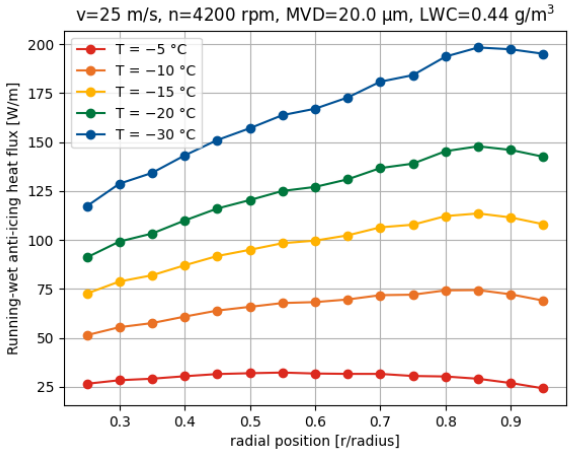

Figure 25: Variation of the heating element integrated heat flux over the span of the propeller for different temperatures at an MVD of 20 µm.

Variation of the anti-icing heat fluxes across meteorological conditions

For the analysis of the required heat fluxes of the running wet and fully evaporative heat fluxes, the required anti-icing heat fluxes calculated by FENSAP-ICE have been integrated over the surface of the propeller. This integration has been performed over the entire surface to create a comparison between the different anti-icing modes, which is not biased by implementation considerations for the different anti-icing modes. A limitation of the integrated area on the leading edge would benefit a running wet system as they usually require heating the entire propeller surface to prevent ice accretion, while for fully evaporative systems only the impingement zones need to be heated. First, the comparison between the running-wet and fully-evaporative modes is presented, then detailed analyses for running-wet simulations are shown.

In Fig. 26, the required running-wet anti-icing heat-flux integrated over the surface of the propeller is shown. The required anti-icing heat flux is very strongly correlated to the temperature. The lowest required anti-icing heat flux is observed at an MVD of 40 µm and at a temperature of −5 °C. The MVD and the LWC have only a minor influence on the required anti-icing heat flux, with a decrease in MVD and an increase in the MVD leading to an increase in the heat fluxes. The heat flux varies by a factor of 8 between the lowest heat flux and the highest heat flux in the simulated conditions. The figure for the CM envelope is in Appendix E. It shows a similar distribution, although the heat fluxes are slightly lower.

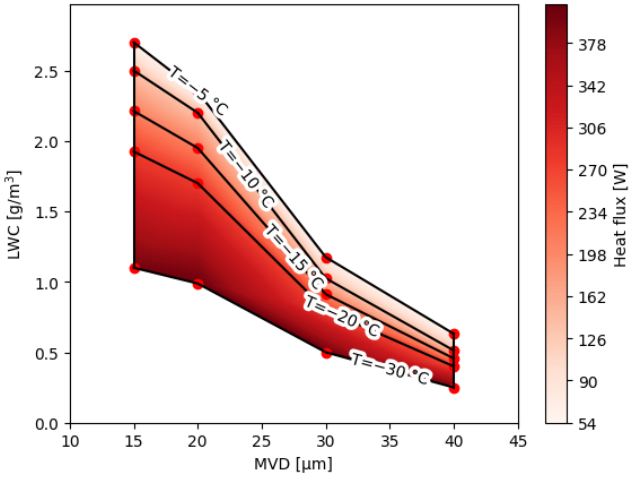

Figure 26: Running-wet heat flux on the propeller over the span of the simulations.

In Fig. 27, the required fully-evaporative heat flux over the simulations in the IM envelope are shown. For the fully evaporative heat flux, the temperatures are much more strongly related to the LWC rather than the temperature. In the selected study points, the minimum required heat-flux is at −30 °C with an MVD of 40 µm. This coincides with the lowest-used LWC. In this condition, the required anti-icing heat flux is lower for a fully evaporative system compared to a running wet design. The highest heat flux is required at −5 °C with an MVD of 20 µm. In this position, the peak heat flux of 1080 W is more than twice the highest running wet heat flux used in this study. Again, the figure for the CM envelope is shown in Appendix D.

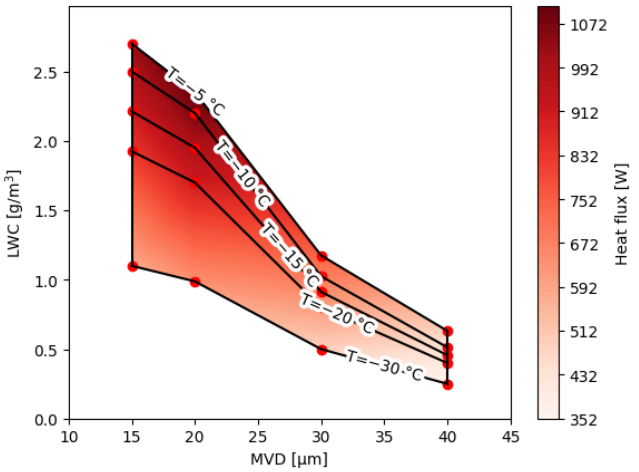

Figure 27: Surface integrated fully-evaporative heat flux on the propeller over the span of the simulations.

The ratio between the running wet and the fully-evaporative heat flux is shown in Fig. 28. Over most of the IM envelope, the running wet anti-icing heat flux is significantly lower than the fully evaporative heat flux, only at a temperature of −30 °C and an MVD of 40 µm would an ideally designed fully evaporative system use less energy than a running-wet system.

The same comparison is shown for the CM envelope in Fig. 29. Here, a fully evaporative system is shown to be more efficient with temperatures of −20 °C and below. Also, the benefit of a running wet system is lower, compared to the IM envelope. The benefit of the running wet system is increasing with an increase in temperature, and a decrease in MVD. The difference between the IM and CM envelope is also showing a significant influence of the LWC on the relative

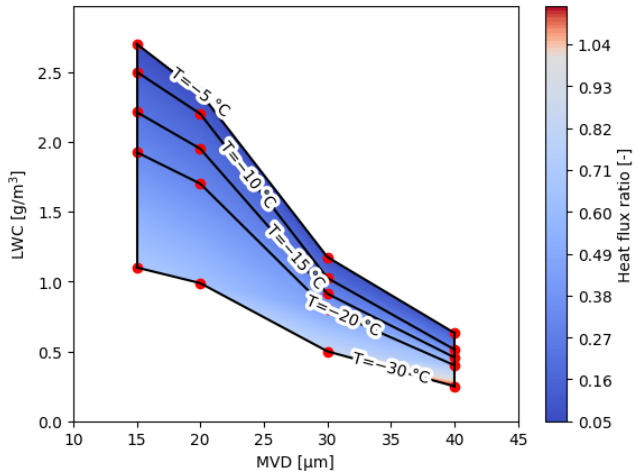

Figure 28: Ratio between the surface integrated required running-wet and fully-evaporative anti-icing heat flux on the entire propeller in IM conditions.

efficiency of the systems. From this analysis follows, that for most conditions, a running wet system is beneficial over a fully evaporative system, and thus the following work is focused on the behavior of a running wet system.

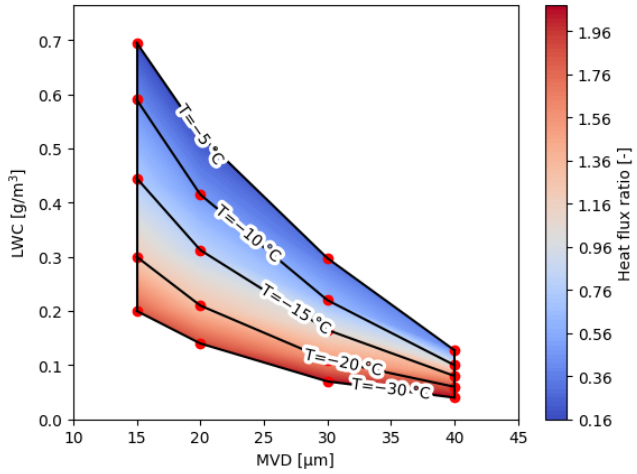

Figure 29: Ratio between the required surface integrated running-wet and fully-evaporative anti-icing heat flux on the entire propeller in CM conditions.

For the design of a robust IPS heating layout, the question of the correlation between the convective heat flux and the other parts of the heat flux is important. This is because if the UAV is leaving a cloud, the sources for the required heat flux caused by the droplets, mainly the energy of the impinging droplets and the evaporative heat flux to evaporate the droplets suddenly do not exist anymore. As the evaporative cooling is removed, suddenly the temperature of the heating element might increase, if the heating power to the propeller is not adjusted immediately. Therefore, the ratio between the required anti-icing heat flux and the convective heat flux can be used to estimate the sensitivity of the system as it exits the cloud and the temperatures in the heater are expected to increase. In Fig. 30, the proportion of the required running wet anti-icing heat flux that is the convective heat flux is shown. The convective heat flux is always the largest part of the running wet anti-icing heat flux, with a share ranging from 60% to 91% of the total heat flux.

In Fig. 31, the peak convective heat flux for the section at 75% of the radius of the propeller is shown, plotted over the simulated temperatures. This is done, as the convective heat flux is independent of the droplet size and LWC, and is thus the same for the CM and IM

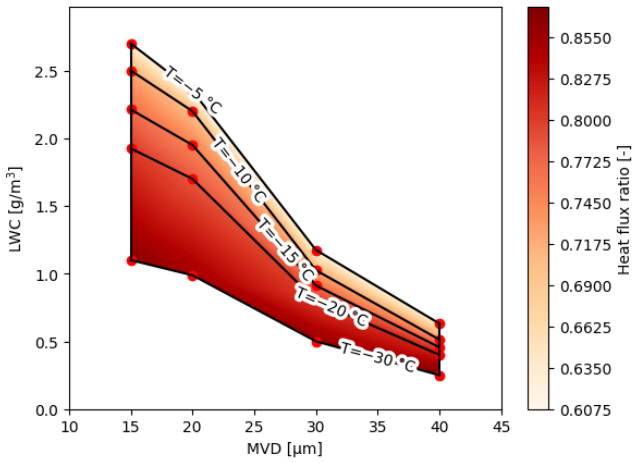

Figure 30: Convective part of the running-wet anti-icing heat flux.

envelope. Additionally, the convective heat flux integrated over the surface of the propeller is shown. It can be seen, that both are linearly dependent on the temperature.

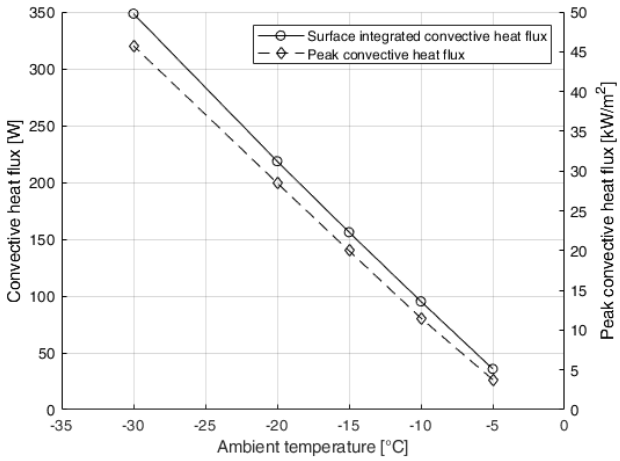

Figure 31: Peak running-wet convective heat flux on the propeller at 75% of the radius over the range of the conditions.

Lastly, in Fig. 32, the ratio between the minimal chordwise peak heat flux and the maximum chordwise peak heat flux on the propeller is shown. It can be seen, that the ratio between the peak heat fluxes on the propeller leading edge is increasing with a decrease in the temperature. For the running wet anti-icing peak heat flux variation between the minimum value and the maximum value is between 1.88 and 2.5. The running wet convective heat flux is showing a similar distribution, with a ratio changing between 1.6 and 2.4. This indicates, that the ratio of the spanwise propeller heat distribution is changing if the UAV is leaving a cloud, with a greater spanwise variation inside the cloud than outside. This bears the risk of overheating the central part of the propeller as the UAV exists the cloud, as suddenly there is a relatively larger heat requirement towards the tip of the propeller than before.

Discussion

Simulation uncertainties

Numerical simulations have multiple sources that could cause inaccuracies. The choice of a fully turbulent turbulence model is based on the assumption that the ice accumulated on the propeller will

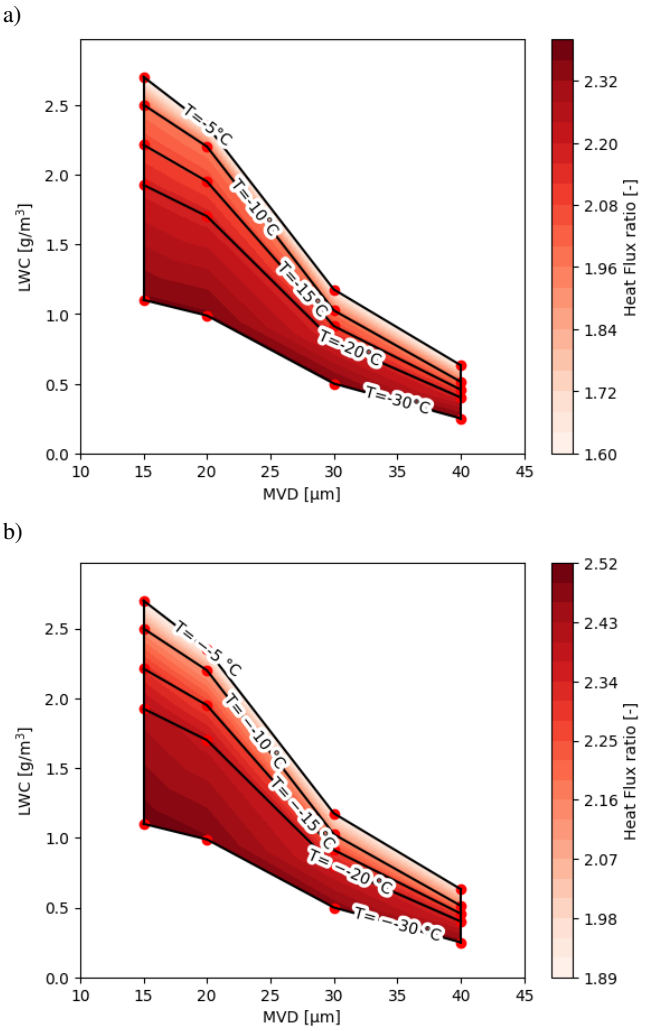

Figure 32: Ratio between the minimal chordwise peak heat flux and the maximum value on the propeller. a) For the convective running wet heat flux. b) For the running wet anti-icing heat flux.

lead to the transition of the laminar boundary layer to a turbulent one, making a turbulent boundary layer appropriate for the simulation of the performance of an iced propeller [13]. For the simulation of the clean performance of the propeller outside of icing conditions, a turbulence model including transition might improve the performance prediction. This does not influence the comparison between different icing conditions, but the simulations might thus underestimate the performance impact of icing conditions relative to a clean propeller.

The second large source of uncertainty is the mesh resolution. For a 3D simulation, the available computational power is limiting the mesh resolution below the theoretical optimal resolution. This is especially affecting simulations with complex and glaze ice shapes since they are not only dependent on the impingement of water but also on the calculated heat fluxes. The mesh convergence study has shown that while the mesh is still dependent on the mesh resolution, the small change between ice shape and aerodynamic performance values between the base and the fine mesh shows a sufficient convergence to assume that the simulations give valid results. Additional sources of uncertainty are the surface roughness implementation in Fensap. Additionally, factors like ice shedding, or changes in the ice density are not implemented in FENSAP-ICE. Thus they cannot be reproduced by the simulations.

A third source influencing the results is the accuracy of the used geometry. Especially for propellers with a chord length in the order of magnitude of a few tens of centimeters, and a thickness of a few millimeters, small geometric inaccuracies in the leading edge geometry will have a large influence on the ice geometry and the predicted heat fluxes. For this reason, it might be useful to not focus on peak heat fluxes but focus on values that are integrated over larger surface areas, like the heating element or the entire surface. This will reduce the influence of small geometric changes on the results.

Ice shape simulation

The ice shapes on the propeller are strongly dependent on the temperature and the LWC of the air, the correlation with the MVD seems to be linked to the change of either the temperature or the LWC if the MVD is changed inside the CM or IM envelopes. The largest ice shapes can be observed at temperatures of −20 °C and an MVD of 15 µm. The ice mass is influenced by the amount of water in the air, the amount of water that is captured by the propeller, and finally the amount of water that is freezing onto the propeller. For different conditions, different factors become dominant. At low temperatures and LWCs, the freezing fraction is one. Meaning that all the droplets impinging on the propeller freeze immediately. In these conditions, the ice mass is equal to the amount of water impinging on the propeller. Therefore, there exists a strong correlation with the LWC in these conditions. At warmer temperatures like −5 °C, the ice mass is dependent on the amount of water freezing on the propeller. This freezing fraction is getting lower with warmer temperatures. Therefore, the peak ice mass is not observed at −5 °C, but at lower temperatures of −15 °C even with the lower LWC at those temperatures.

The different temperatures also have an influence on the ice shapes. If the freezing fraction is lower than one, there is a chance of horns forming on the surface of the propeller. Those horns will then have a significant influence on the performance of the propeller. The comparison between the freezing fraction in CM and IM conditions shows that the higher LWCs in IM conditions lead to lower freezing fractions, where even at −30 °C, the freezing fraction on the leading edge of the airfoil is not 1. This can be correlated to the ice shapes in IM conditions, which show fewer streamwise ice shapes at the same temperatures as comparable CM conditions. Therefore, only the −5 °C cases show horn shapes at 75% of the radius of the propeller.

Performance degradation

The performance of the propeller is also strongly dependent on the meteorological conditions. In the simulations, the thrust of the propeller is more strongly influenced by the ice accretion than the torque of the propeller. The maximum thrust decrease of the propeller in IM conditions occurs at −10 °C with the maximum torque increase at −15 °C. The minimum thrust decrease can be found at the lowest analyzed temperature of −30 °C and the highest MVD of 40 µm. In these conditions, the thrust is increased relative to the clean propeller. This could be due to the streamwise ice shape that is created under those conditions. The torque increase caused by the larger induced drag as well as due to the rougher surface leads to an overall loss of efficiency even at those conditions. The fact that this specific point is the most critical can also be linked to the lowest LWC at this point, which at the freezing fraction of one leads to the smallest ice mass.

An important factor that is not modeled in the ice shape calculations is ice shedding. For this reason, the performance of the propeller after prolonged exposure to icing conditions differs from the presented results. If the numerical results are compared to the experimental data collected in earlier studies, the predicted performance degradation of the propeller is the strongest at very low temperatures during the experimental campaign, and for CM conditions, the warmest tested temperature of −5 °C has the strongest performance degradation, and in IM conditions, −15 °C is showing the strongest performance

degradation. Since the total performance degradation is strongly dependent on the ice shedding in the experimental campaign, a better comparison is the gradient of the performance degradation. In which a previous experimental campaign [23] is predicting the strongest gradient at −10 °C. The experimental campaign was conducted at a constant LWC of 0.44 g/m^3, which correlates closely to the CM LWC at −10 °C. In this case, the experimental campaign shows the strongest performance degradation gradient at −10 °C. In the comparable simulations, the strongest performance degradation is at −5 °C. This could be due to the higher LWC at −5 °C compared to the experiment, which leads to an increase of the ice mass and might lead to a lower freezing fraction and, thus, more horn shapes which influence the performance negatively. This highlights the need to analyze the experimental and numerical data carefully, as different conditions might lead to very different conclusions about the severity of different icing conditions. Compared to the experimental data, the advantage of the numerical analysis is the ability to test a wide range of conditions and the freedom from the limitations of the IWT. Conversely, the IWT is able to incorporate additional effects like ice shedding, which are not yet implemented in the numerical models.

Anti-icing loads

The chordwise heat flux distribution contains a high peak that falls off rapidly after the stagnation point. This would indicate the need to implement a small heating zone with a high heat flux on the leading edge of the propeller. This could be supplemented by a weaker secondary heating zone on the top of the propeller. This second heating zone would be used to prevent the water running back from the main heating zone from freezing on the propeller.

The spanwise change of the heat flux of the propeller can be separated into an increase in the peak heat flux and a change in the total heat flux required. The nonlinear change in the peak heat flux in the area of changing airfoils between 65% and 80% of the airfoil leads to the question if the peak heat flux is the best metric to estimate the required heat flux for the propeller of a UAV. Therefore, a look at the integrated heat flux over a virtual heating element could be more useful for the design of the propeller IPS. The simulations show that the variations of the integrated heat flux with the span of the propeller are lower than the change of the peak heat flux. Therefore, the need to implement multiple spanwise zones might be reduced if wider heating zones are used.

The comparison of the running wet heat flux across different points in Appendix C CM and IM envelopes highlights that the heat flux is most strongly correlated to the change in temperature. Conversely, the fully evaporative anti-icing heat fluxes are mostly dependent on the liquid water content. In most conditions, especially in the IM envelope, the running wet heat flux on the propeller is significantly lower than the required heat flux for a fully evaporative system. Therefore, it would be more beneficial to implement a running wet system on a propeller, even if the prevention of water freezing beyond the protected areas might then require heating most if not all, of the surfaces on the propeller.

This data can be used to design an optimal IPS system for a propeller. The chordwise distribution of the heat fluxes can be used to create a template for the layout of an optimal IPS system on a propeller. A possible suggestion would be to use two chordwise heating zones. One main zone to cover an area of 75% or more of the heat flux, and a secondary heating zone to cover the areas with 25% or more of the heat flux on the top surface of the propeller.

The critical cases for the design of an IPS can be found at the extremes of the design envelope. The two main influencing factors on the required heat flux of the IPS are the convective heat flux and the evaporative heat flux. For the design of an ETIPS, the convective heat flux has special importance as it is the only heat flux to remain if the UAV leaves the cloud. The convective heat flux required for anti-icing is dependent on the temperature of the air. This value is going to be the highest at very low temperatures, while it is going to find its minimum at the highest considered temperatures.

A possible IPS system could incorporate two heating zones. The primary zone covers the peak heat flux on the leading edge of the propeller. This zone needs to produce a heat flux larger than the required anti-icing load on the leading edge of the propeller over the entire span of the propeller. A proposed solution could be to use a heating zone that has the same amount of resistance per meter but is changing its width to encompass the rising heat flux requirements. By making the width inversely proportional to the required peak heat flux, this zone will be able to prevent ice accretion on the propeller. The secondary zone could be designed similarly, and cover the entire area up to the point of 25% of the required heat flux on top of the propeller.

Further heating zones to cover the entire impingement zone on the top of the propeller and to cover the secondary impingement zone on the lower surface of the propeller could be included in further iterations of the design.

With the high heat fluxes required for an anti-icing system, accurate control of the system is important to prevent overheating of the material and to keep the efficiency as high as possible. The required heat flux on a running wet system is mainly dependent on the temperature. Therefore, an accurate measurement of the outside air temperature is essential to the control of an IPS system. The required peak heat flux is changing by a factor larger than 5, and the power requirement over the entire surface is changing by a factor larger than 8. Without accurate information on the environmental conditions, this would likely lead to issues in the system, if it were to be operated without implementing a controller based on the meteorological conditions. A helpful point for the design of a running wet system is that the ratio between the chordwise peak heat flux on the propeller across the span of the rotor is similar to the anti-icing heat flux and the convective heat flux. Therefore, the required heat flux distribution is only changing by a low ratio if the UAV leaves a cloud with an activated ETIPS. The fact that the ratio is increasing with a decrease in temperature and MVD means that for an ETIPS design, the case with the minimal MVD and temperature of the design envelope should be chosen as a critical point for the heat flux ratio across the span of the propeller.

Conclusion

The analysis shows the influence of different meteorological conditions on the ice accretion on the UAV. It shows a large dependency of the ice shapes on the temperature of the ice accretion and the liquid water content. Droplet size appears of lesser importance within the IM and CM envelope but might play a more significant role in different meteorological conditions, like supercooled large droplet icing. Similarly, the influence of icing on the performance of UAV propellers is strongly dependent on the meteorological conditions. The required heat fluxes for a propeller of a UAV have been computed. This was used to analyze the change in the required heat fluxes of a propeller of a UAV over the intermittent maximum conditions of Appendix C. This showed that the heat fluxes on the propeller of a small UAV are showing a large variation spanwise and chord-wise.

The following critical points for the propeller of a UAV in IM icing conditions could be identified. The maximum ice accretion is occurring at the highest calculated temperature of −5 °C and the minimal MVD of 15 µm in CM conditions. In IM conditions, the peak ice mass occurs at a temperature of −10 °C and the minimal MVD of 20 µm. The fastest thrust degradation can be observed at the same conditions for CM conditions. In IM conditions, the peak torque increase is also occurring at the same temperature as the peak in ice mass, but the worst case for the thrust loss is at −15 °C and an MVD of 20 µm. The efficiency degradation is dominated by thrust loss. For

CM conditions, in the most severe case, the propeller stopped producing thrust after 160 s of ice accretion. This performance degradation is more severe compared to the performance degradation that occurs on wings of comparable UAVs, and it is occurring at slightly lower temperatures.

For anti-icing heat loads, the critical design points are on the edge of the design envelopes. For running wet systems, the peak required anti-icing heat flux is at the minimal temperature of the envelope, at the minimal analyzed MVD. At these conditions, the spanwise variation of the heat fluxes is also the largest. Conversely, at the minimal analyzed temperature and maximal MVD, the required heat fluxes are the lowest. Hence, for a design with a minimal selection of analyzed temperatures, those two conditions could be chosen as critical design points.

A fully evaporative system will, in most IM conditions, use significantly more energy than a running wet system, but it has an efficiency advantage at temperatures below −15 °C in CM conditions. Thus, it might be sensible to operate a propeller IPS in a fully evaporative mode in those conditions. To design a fully evaporative system, the most critical design point is at the highest operational temperature, and lowest MVD, which represents the maximum required energy, and at the lowest temperature and the maximal MVD to get the critical design point for the lowest required power.

Further steps in the research are the validation of the calculated ice shapes and performance numbers against experimental data. Furthermore, a propeller with an IPS is being developed, which could be used in an effort to validate the anti-icing loads.

References

1. H. Shakhatreh, A. H. Sawalmeh, A. Al-Fuqaha, Z. Dou, E. Almaita, I. Khalil, N. S. Othman, A. Khreishah, and M. Guizani, "Unmanned Aerial Vehicles (UAVs): A Survey on Civil Applications and Key Research Challenges," *IEEE Access*, vol. 7, pp. 48572–48634, 2019.

2. K. L. Sørensen, K. Borup, R. Hann, B. Bernstein, and M. Hansbø, "UAV Atmospheric Icing Limitations," tech. rep., research report, 2021.

3. B. C. Bernstein, C. A. Wolff, and F. McDonough, ""An Inferred Climatology of Icing Conditions Aloft, Including Supercooled Large Drops. Part I: Canada and the Continental United States"," *Journal of Applied Meteorology and Climatology*, vol. 46, no. 11, pp. 1857 – 1878, 2007.

4. B. C. Bernstein and C. L. Bot, ""An Inferred Climatology of Icing Conditions Aloft, Including Supercooled Large Drops. Part II: Europe, Asia, and the Globe"," *Journal of Applied Meteorology and Climatology*, vol. 48, no. 8, pp. 1503 – 1526, 2009.

5. K. Szilder and W. Yuan, "In-Flight Icing on Unmanned Aerial Vehicle and its Aerodynamic Penalties," in *Progress in Flight Physics*, vol. 9, pp. 173–188, 01 2017.

6. R. Hann and T. Johansen, "Unsettled Topics in Unmanned Aerial Vehicle Icing," *SAE International, SAE EDGE Research Report EPR2020008*, 2020.

7. R. W. Gent, N. P. Dart, and J. T. Cansdale, "Aircraft Icing," *Philosophical Transactions: Mathematical, Physical and Engineering Sciences*, vol. 358, no. 1776, pp. 2873–2911, 2000.

8. Y. Cao, W. Tan, and Z. Wu, "Aircraft icing: An ongoing threat to aviation safety," *Aerospace Science and Technology*, vol. 75, p. 353–385, 2018.

9. K. Szilder and S. McIlwain, "In-Flight Icing of UAVs - The Influence of Reynolds Number on the Ice Accretion Process," *SAE Technical Paper 2011-01-2572*, 2011.

10. N. Fajt, R. Hann, and T. Lutz, "The Influence of Meteorological Conditions on the Icing Performance Penalties on a UAV Airfoil," *8th European Conference for Aeronautics and Space Sciences (EUCASS)*, 2019.

11. R. Hann, R. J. Hearst, L. R. Sætran, and T. Bracchi, "Experimental and Numerical Icing Penalties of an S826 Airfoil at Low Reynolds Numbers," *Aerospace*, vol. 7, no. 4, p. 46, 2020.

12. N. Williams, A. Benmeddour, G. Brian, and M. Ol, "The effect of icing on small unmanned aircraft low reynolds number airfoils," in *In: 17th Australian International Aerospace Congress : AIAC 2017. Barton, A.C.T.: Engineers Australia, Royal Aeronautical Society, 2017: 19-25.*, 2017.

13. R. Hann, *UAV Icing: Challenges for computational fluid dynamic (CFD) tools*. ICCFD11, 2022.

14. Y. Liu, L. Li, Z. Ning, W. Tian, and H. Hu, "Experimental Investigation on the Dynamic Icing Process over a Rotating Propeller Model," *Journal of Propulsion and Power*, vol. 34, no. 4, pp. 933–946, 2018.

15. Y. Liu, L. Li, W. Chen, W. Tian, and H. Hu, "An Experimental Study on the Aerodynamic Performance Degradation of a UAS Propeller Model Induced by Ice Accretion Process," *Experimental Thermal and Fluid Science*, vol. 102, pp. 101–112, 2019.

16. N. C. Müller, R. Hann, and T. Lutz, "Uav icing: Numerical simulation of propeller ice accretion," in *AIAA AVIATION 2021 FORUM*, 2021.

17. G. Zhao, Q. jun Zhao, and X. Chen, "New 3-D Ice Accretion Method of Hovering Rotor including Effects of Centrifugal Force," *Aerospace Science and Technology*, vol. 48, pp. 122–130, 2016.

18. Y. Cao and K. Chen, "Helicopter Icing," *The Aeronautical Journal*, vol. 114, no. 1152, p. 83–90, 2010.

19. C. Hochart, G. Fortin, J. Perron, and A. Ilinca, "Wind Turbine Performance under Icing Conditions," *Wind Energy: An International Journal for Progress and Applications in Wind Power Conversion Technology*, vol. 11, no. 4, pp. 319–333, 2008.

20. O. Yirtici, S. Ozgen, and I. H. Tuncer, "Predictions of Ice Formations on Wind Turbine Blades and Power Production Losses due to Icing," *Wind Energy*, vol. 22, no. 7, pp. 945–958, 2019.

21. S. Yan, T. I. Opazo, J. W. Langelaan, and J. L. Palacios, "Experimental Evaluation and Flight Simulation of Coaxial-rotor Vehicles in Icing Clouds," *Journal of the American Helicopter Society*, 2019.

22. S. Nilamdeen, Y. Zhang, I. Ozcer, and G. S. Baruzzi, "An ice shedding model for rotating components," *SAE Technical Paper Series*, 2019.

23. N. C. Müller and R. Hann, "UAV Icing: A Performance Model for a UAV Propeller in Icing Conditions," in *AIAA AVIATION 2022 Forum*, AIAA, 2022.

24. J. Anthony and W. G. Habashi, "Helicopter rotor ice shedding and trajectory analyses in forward flight," *Journal of Aircraft*, vol. 58, no. 5, pp. 1051–1067, 2021.

25. K. Itagaki, "Mechanical Ice Release Processes. I. Self-Shedding from High-Speed Rotors," *Technical report ADA135369, COLD REGIONS RESEARCH AND ENGINEERING LAB HANOVER NH*, 1983.

26. Federal Aviation Administration (FAA), "Part I – Atmospheric Icing Conditions," *Title 14 CFR Part 25 Appendix C, Doc. No. 4080, 29 FR 17955, Amdt. 25-140, 79 FR 65528*, 11 2014.

27. A. R. Hovenburg, F. A. de Alcantara Andrade, R. Hann, C. D. Rodin, T. A. Johansen, and R. Storvold, "Long-range path planning using an aircraft performance model for battery-powered suas equipped with icing protection system," *IEEE Journal on Miniaturization for Air and Space Systems*, vol. 1, no. 2, p. 76–89, 2020.

28. A. R. Hovenburg, F. A. de Alcantara Andrade, R. Hann, C. D. Rodin, T. A. Johansen, and R. Storvold, "Long-range path planning using an aircraft performance model for battery-powered suas equipped with icing protection system," *IEEE Journal on Miniaturization for Air and Space Systems*, vol. 1, no. 2, p. 76–89, 2020.

29. S. K. Thomas, R. P. Cassoni, and C. D. MacArthur, "Aircraft Anti-Icing and De-Icing Techniques and Modeling," *Journal of Aircraft*, vol. 33, no. 5, pp. 841–854, 1996.

30. Y. Liu, L. Li, H. Li, and H. Hu, "An Experimental Study of Surface Wettability Effects on Dynamic Ice Accretion Process over an UAS Propeller Model," *Aerospace Science and Technology*, vol. 73, pp. 164–172, 2018.

31. N. Han, H. Hu, and H. Hu, "An Experimental Investigation to Assess the Effectiveness of Various Anti-Icing Coatings for UAV Propeller Icing Mitigation," in *AIAA AVIATION 2022 Forum*, AIAA, 2022.

32. E. Villeneuve, A. Samad, C. Volat, M. Béland, and M. Lapalme, "Experimental Investigation of Icing Effects on a Hovering Drone Rotor Performance," *Drones*, vol. 6, no. 11, p. 345, 2022.

33. R. Hann, K. Borup, A. Zolich, K. Sorensen, H. Vestad, M. Steinert, and T. Johansen, "Experimental Investigations of an Icing Protection System for UAVs," *SAE Technical Paper 2019-01-2038*, 2019.

34. J. Wallisch and R. Hann, "UAV Icing: Experimental Investigation of Ice Shedding Times with an Electrothermal De-Icing System," in *AIAA AVIATION 2022 Forum*, AIAA, 2022.

35. N. Karpen, S. Diebald, F. Dezitter, and E. Bonaccurso, "Propeller-Integrated Airfoil Heater System for Small Multirotor Drones in Icing Environments: Anti-Icing Feasibility Study," *Cold Regions Science and Technology*, vol. 201, p. 103616, 2022.

36. J. Wallisch and R. Hann, "UAV Icing: Intercycle Ice Effects on Aerodynamic Performance," 2023. (submitted).

37. A. Samad, E. Villeneuve, C. Blackburn, F. Morency, and C. Volat, "An Experimental Investigation of the Convective Heat Transfer on a Small Helicopter Rotor with Anti-Icing and De-Icing Test Setups," *Aerospace*, vol. 8, no. 4, 2021.

38. Mejzlik, "Propeller 21X13 CCW 2B E - Mejzlik Propellers," *shop.mejzlik.eu*, 2021. (Accessed 02.11.2021).

39. G. S. Baruzzi, W. G. Habashi, J. G. Guevremont, and M. M. Hafez, "A Second Order Finite Element Method for the Solution of the Transonic Euler and Navier-Stokes Equations," *International Journal for Numerical Methods in Fluids*, vol. 20, no. 8-9, p. 671–693, 1995.

40. Y. Bourgault, Z. Boutanios, and W. G. Habashi, "Three-Dimensional Eulerian Approach to Droplet Impingement Simulation using FENSAP-ICE, Part 1: Model, Algorithm, and Validation," *Journal of Aircraft*, vol. 37, no. 1, p. 95–103, 2000.

41. Y. Bourgault, W. G. Habashi, J. Dompierre, and G. S. Baruzzi, "A Finite Element Method Study of Eulerian Droplets Impingement Models," *International Journal for Numerical Methods in Fluids*, vol. 29, no. 4, p. 429–449, 1999.

42. Y. Bourgault, W. Habashi, and H. Beaugendre, "Development of a Shallow Water Icing Model in FENSAP-ICE," *37th Aerospace Sciences Meeting and Exhibit*, 1999.

43. H. Beaugendre, F. Morency, and W. G. Habashi, "FENSAP-Ice's Three-Dimensional In-Flight Ice Accretion Module: ICE3D," *Journal of Aircraft*, vol. 40, no. 2, p. 239–247, 2003.

44. B. L. Messinger, "Equilibrium Temperature of an Unheated Icing Surface as a Function of Air Speed," *Journal of the Aeronautical Sciences*, vol. 20, no. 1, p. 29–42, 1953.

45. I. Ozcer, D. Switchenko, G. S. Baruzzi, and J. Chen, "Multi-Shot Icing Simulations with Automatic Re-Meshing," in *International Conference on Icing of Aircraft, Engines, and Structures*, SAE International, jun 2019.

46. R. Hann, *Atmospheric ice accretions, aerodynamic icing penalties, and ice protection systems on unmanned aerial vehicles, Chapter 7.7*. PhD thesis, Norwegian University of Science and Technology, 2020.

47. B. Løw-Hansen, E. M. L. Coates, N. C. Müller, T. A. Johansen, and R. Hann, "Identification of an Electric UAV Propulsion System in Icing Conditions," tech. rep., SAE Icing Conference, 2023. (submitted).

Contact Information

Nicolas Carlo Müller, M.Sc.
nicolas.c.muller@ntnu.no
Richard Hann, Ph.D.
richard.hann@ntnu.no

Acknowledgments

The work is partly sponsored by the Research Council of Norway through the Centre of Excellence funding scheme, project number 223254, AMOS, and an Industrial Ph.D. with project number 321667, project BIA Rotors with project number 296228, and project IKTPLUSS with project number 316425. We also thank Mejzlik for their cooperation.

Parts of the numerical simulations where performed on the resources provided by the National Infrastructure for High Performance Computing and Data Storage in Norway (UNINETT Sigma2) on the Fram supercomputer, under project number NN9613K Notur/NorStore.

Definitions, Acronyms, Abbreviations

AOA	Angle of attack
CFD	Computational fluid dynamics
CM	Continuous maximum
ETIPS	Electro thermal ice protection system
IM	Intermittent maximum
IPS	Ice protection system
IWT	Icing wind tunnel
LWC	Liquid water content
MVD	Mean volumetric diameter
RANS	Reynolds-averaged Navier–Stokes

APPENDIX A

Table 2: Simulation runs for the intermittent maximum calculations, the simulation duration for each run is 30 s.

Run	MVD [µm]	Temperature [°C]	LWC [g/m^3]
1	15	−5	2.70
2	15	−10	2.50
3	15	−15	2.21
4	15	−20	1.93
5	15	−30	1.10
6	20	−5	2.35
7	20	−10	2.20
8	20	−15	1.95
9	20	−20	1.70
10	20	−30	0.99
11	30	−5	0.99
12	30	−10	1.03
13	30	−15	0.91
14	30	−20	0.80
15	30	−30	0.50
16	40	−5	0.63
17	40	−10	0.51
18	40	−15	0.46
19	40	−20	0.40
20	40	−30	0.25

Table 3: Simulation runs for the continuous maximum calculations, the simulation duration for each run is 180 s.

Run	MVD [µm]	Temperature [C]	LWC [g/m^3]
1	15	−5	0.70
2	15	−10	0.59
3	15	−15	0.45
4	15	−20	0.30
5	15	−30	0.20
6	20	−5	0.53
7	20	−10	0.42
8	20	−15	0.31
9	20	−20	0.21
10	20	−30	0.14
11	30	−5	0.30
12	30	−10	0.22
13	30	−15	0.17
14	30	−20	0.11
15	30	−30	0.07
16	40	−5	0.13
17	40	−10	0.10
18	40	−15	0.08
19	40	−20	0.06
20	40	−30	0.04

APPENDIX B

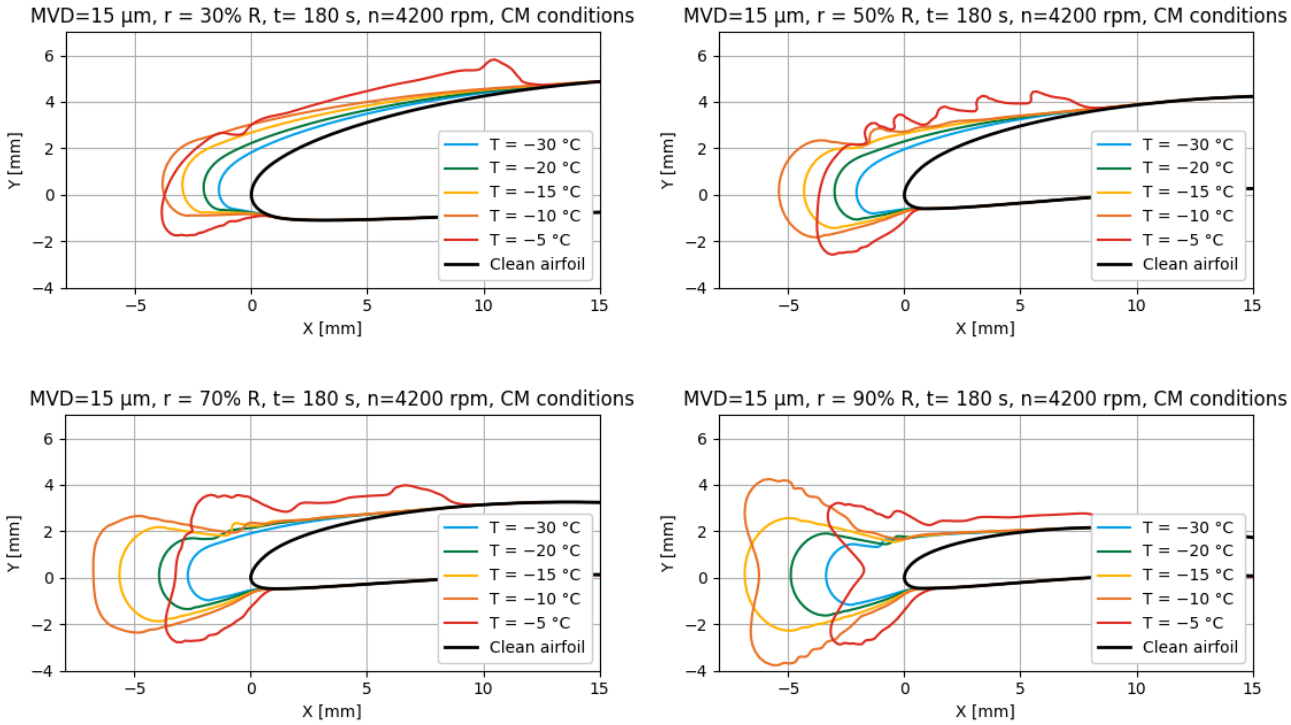

Figure 33: Ice shapes on the propeller for 3D simulations in CM conditions after 180 s of ice accretion.

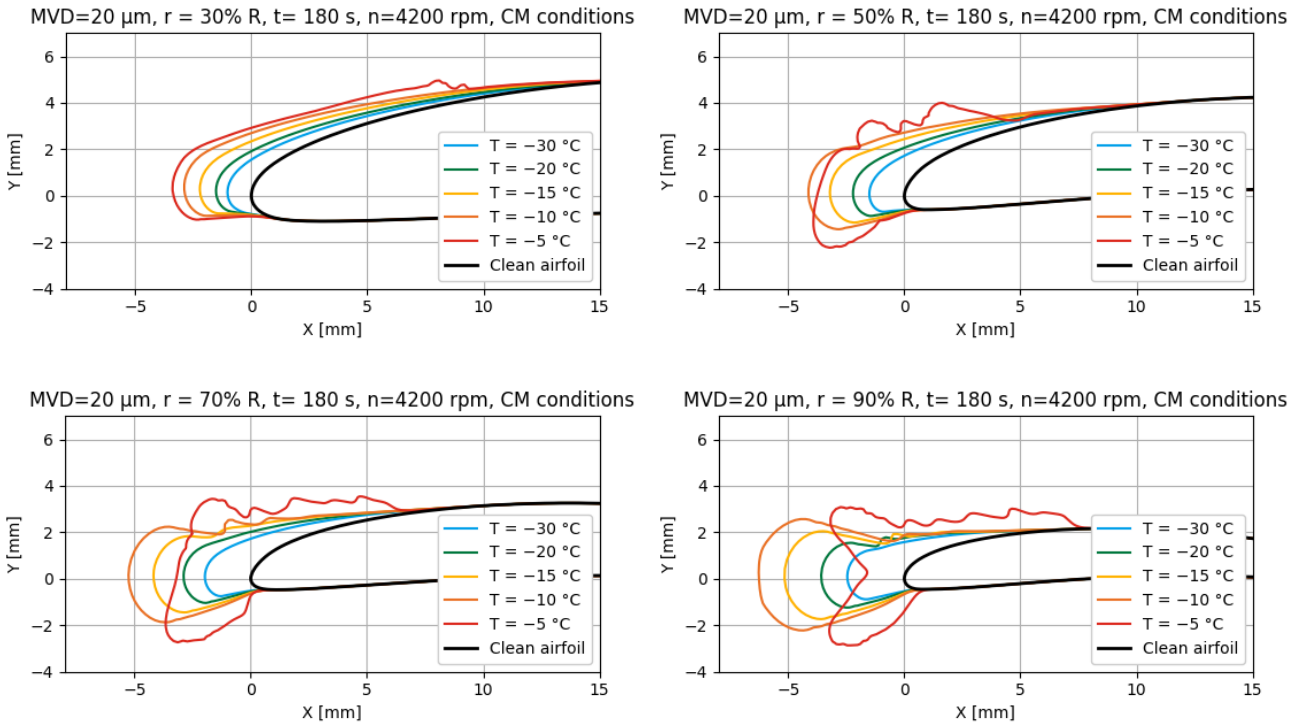

Figure 34: Ice shapes on the propeller for 3D simulations in CM conditions after 180 s of ice accretion.

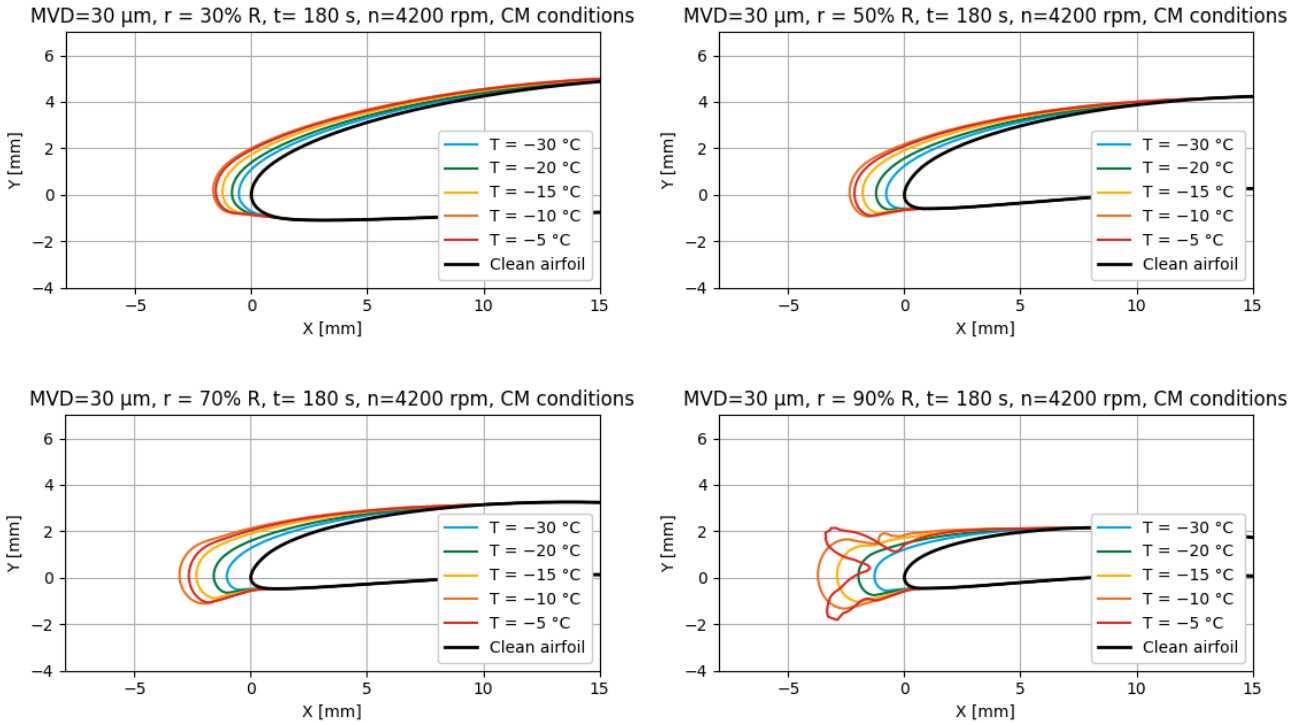

Figure 35: Ice shapes on the propeller for 3D simulations in CM conditions after 180 s of ice accretion.

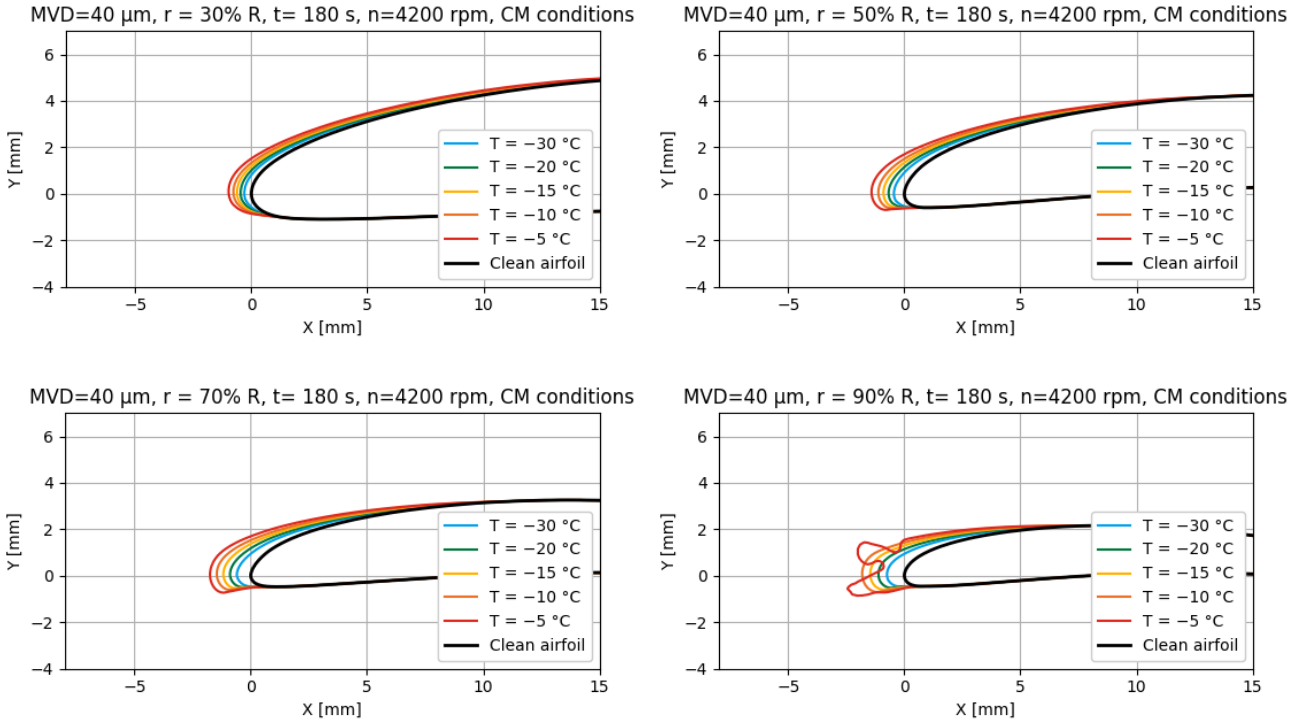

Figure 36: Ice shapes on the propeller for 3D simulations in CM conditions after 180 s of ice accretion.

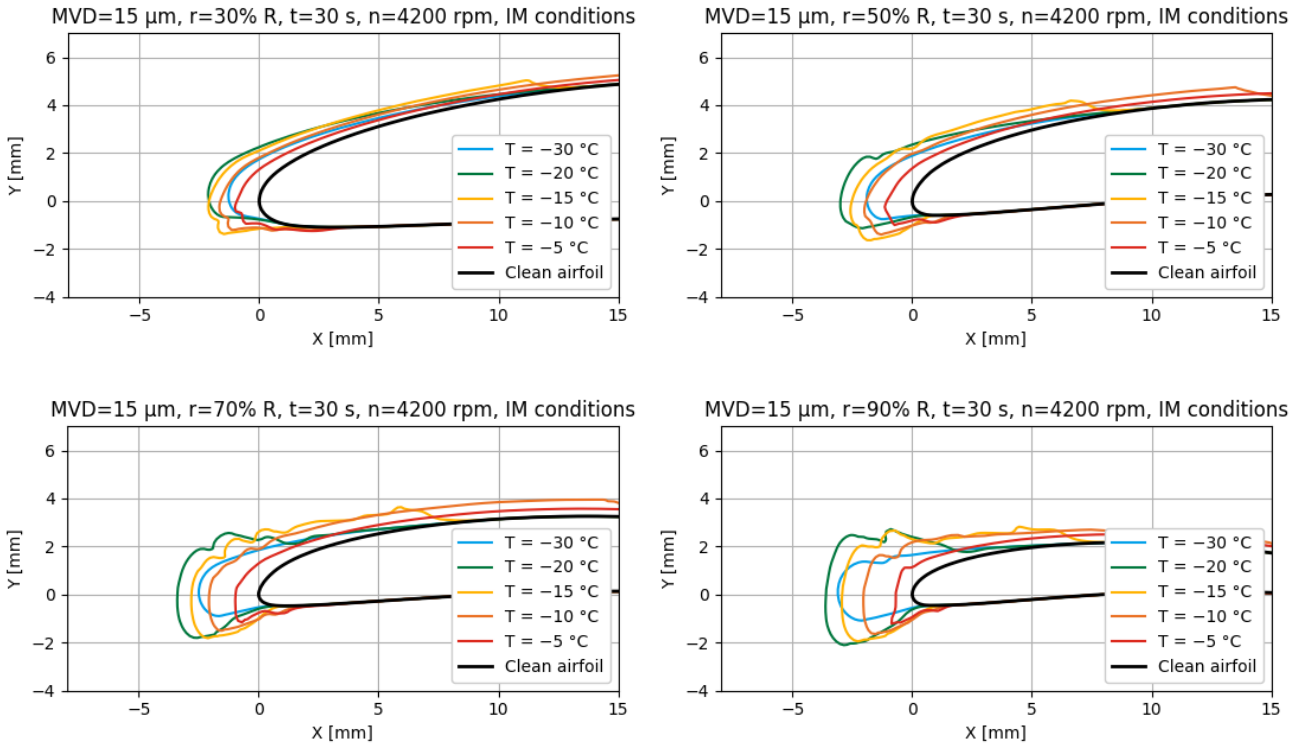

Figure 37: Ice shapes on the propeller for 3D simulations in IM conditions after 30 s of ice accretion.

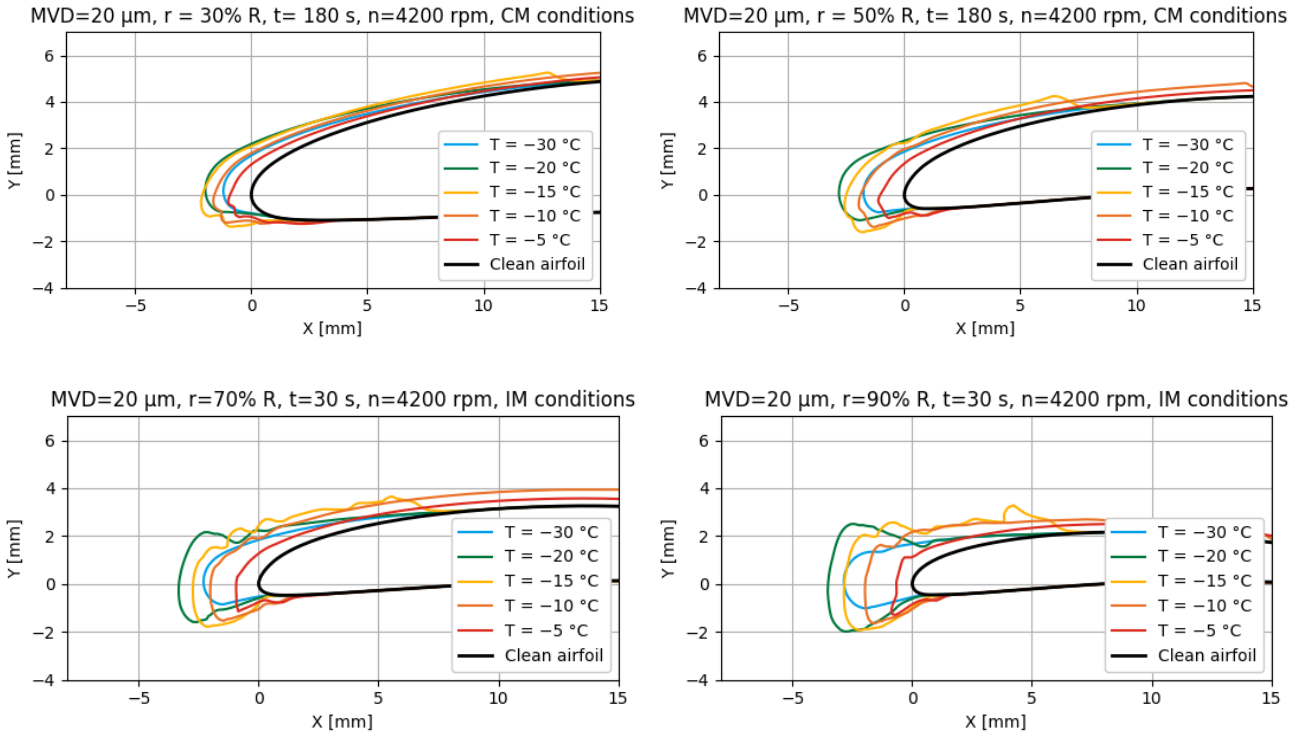

Figure 38: Ice shapes on the propeller for 3D simulations in IM conditions after 30 s of ice accretion.

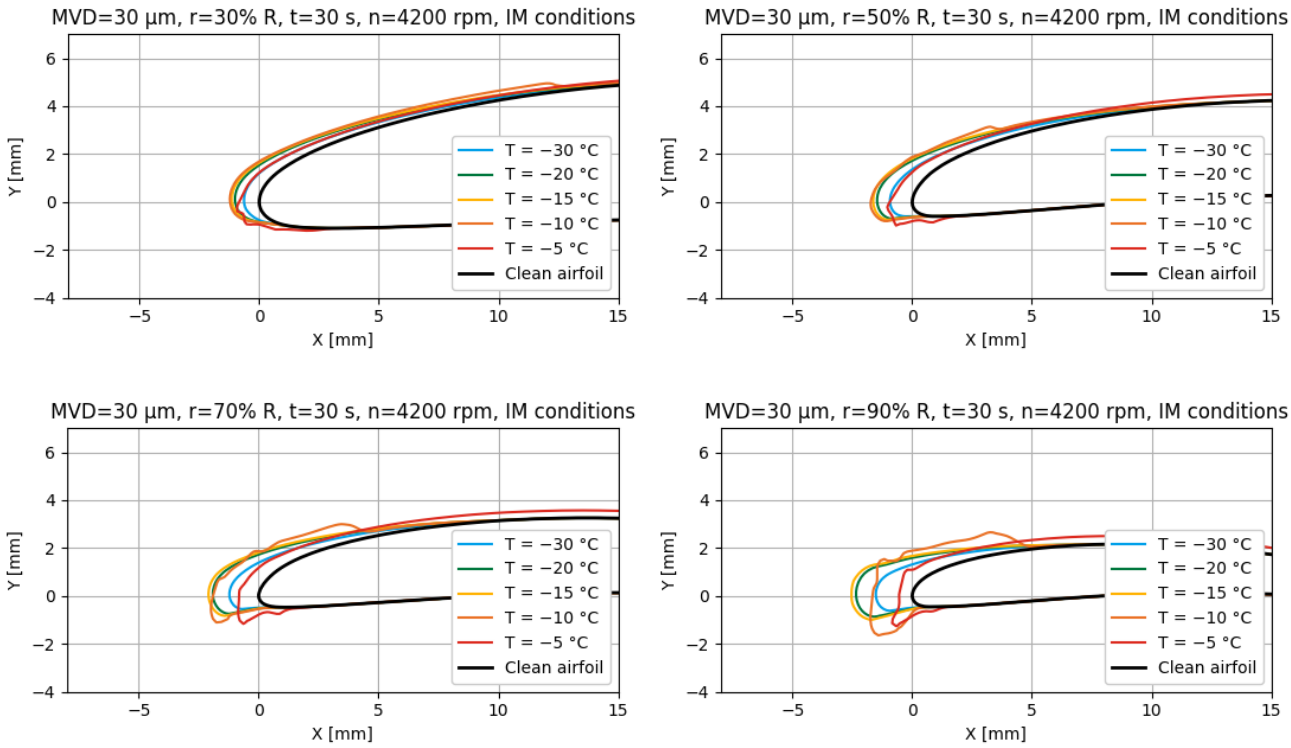

Figure 39: Ice shapes on the propeller for 3D simulations in IM conditions after 30 s of ice accretion.

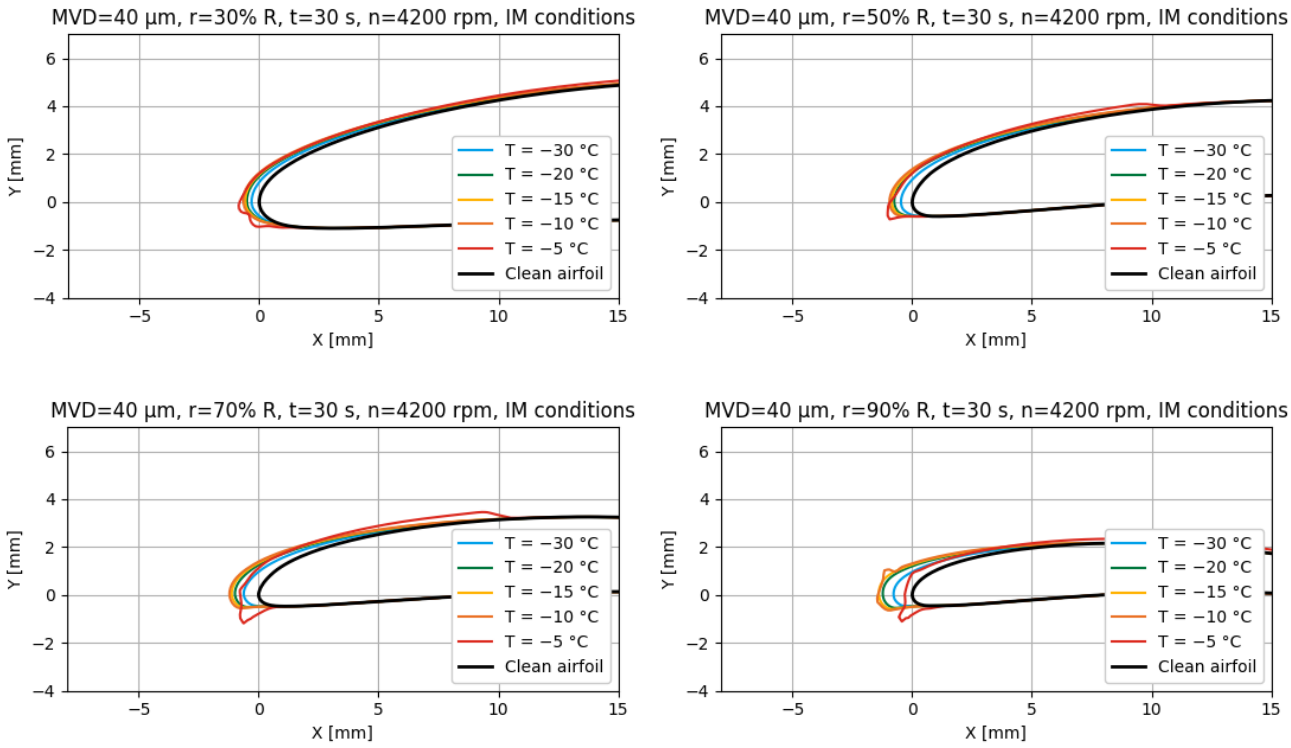

Figure 40: Ice shapes on the propeller for 3D simulations in IM conditions after 30 s of ice accretion.

APPENDIX C

Intermittent maximum

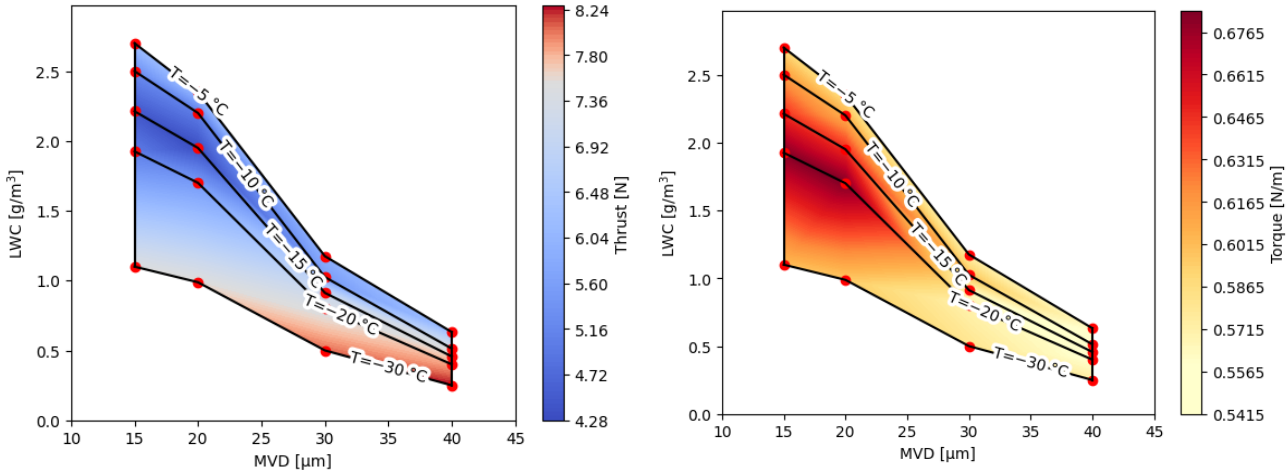

Continuous maximum

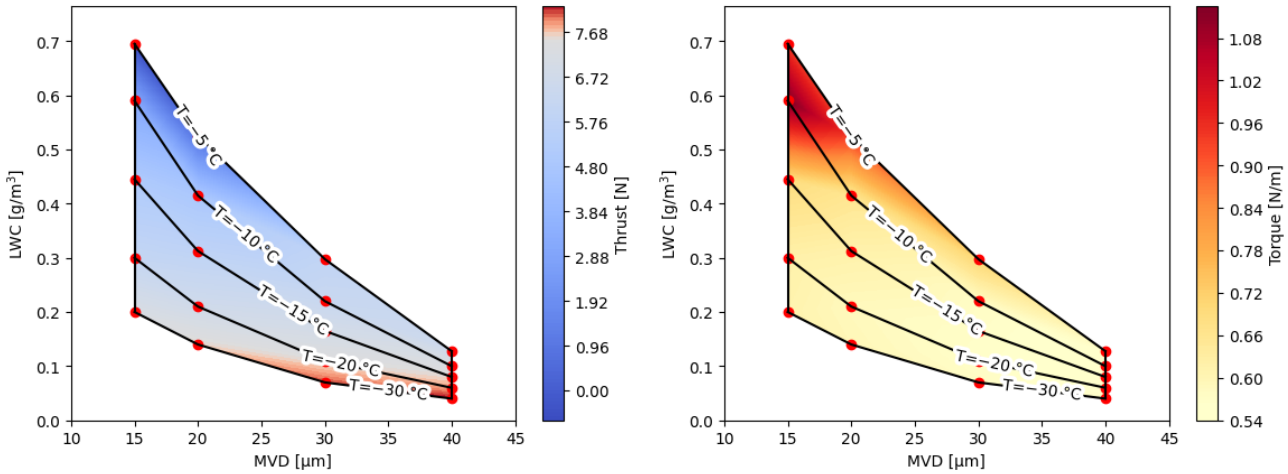

Figure 41: Thrust and torque results on the propeller after 30 s of ice accretion in IM conditions and 180 s in CM conditions

APPENDIX D

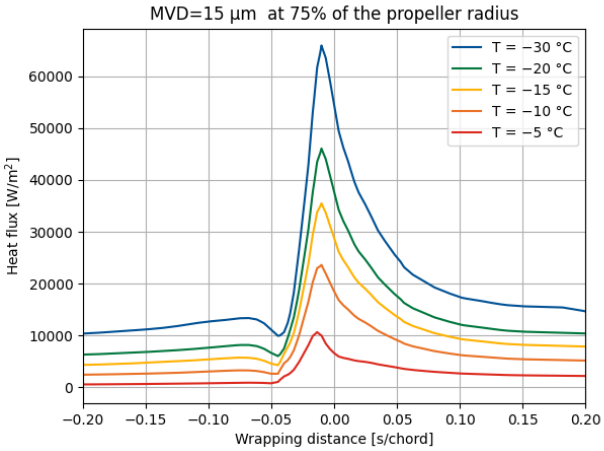

Figure 42: Running-wet heat flux on the propeller for cases with an MVD of 15 µm in the CM envelope.

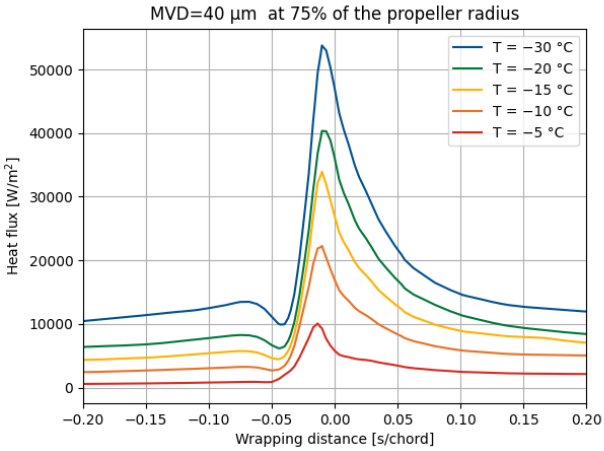

Figure 43: Running-wet heat flux on the propeller for cases with an MVD of 40 µm in the CM envelope.

APPENDIX E

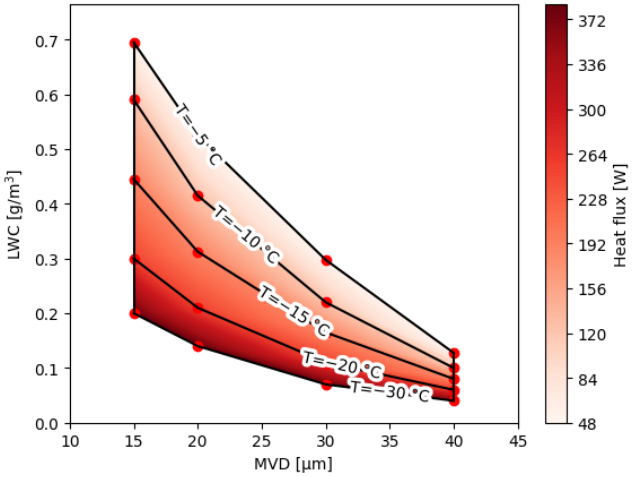

Figure 44: Running-wet heat flux in CM conditions on the propeller over the span of the simulations

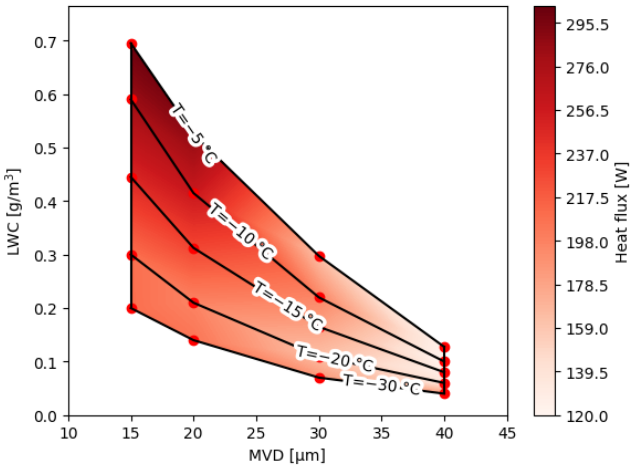

Figure 45: Fully-evaporative heat flux in CM conditions on the propeller over the span of the simulations